7266 *Inorg. Chem.* **2010**, *49*, 7266–7281
DOI: 10.1021/ic902051t

Inorganic Chemistry
Article

Density Functional Theory Analysis of Structure, Energetics, and Spectroscopy for the Mn−Fe Active Site of *Chlamydia trachomatis* Ribonucleotide Reductase in Four Oxidation States

Wen-Ge Han,[†] Debra Ann Giammona,[‡] Donald Bashford,[‡] and Louis Noodleman*[,†]

[†]*Department of Molecular Biology, TPC15, The Scripps Research Institute, 10550 North Torrey Pines Road, La Jolla, California 92037, and* [‡]*Structural Biology, St. Jude Children's Research Hospital, 262 Danny Thomas Place, Memphis, Tennessee 38105*

Received October 15, 2009

Models for the Mn−Fe active site structure of ribonucleotide reductase (RNR) from pathogenic bacteria *Chlamydia trachomatis* (*Ct*) in different oxidation states have been studied in this paper, using broken-symmetry density functional theory (DFT) incorporated with the conductor like screening (COSMO) solvation model and also with finite-difference Poisson−Boltzmann self-consistent reaction field (PB-SCRF) calculations. The detailed structures for the reduced Mn(II)−Fe(II), the met Mn(III)−Fe(III), the oxidized Mn(IV)−Fe(III) and the superoxidized Mn(IV)−Fe(IV) states are predicted. The calculated properties, including geometries, ^{57}Fe Mössbauer isomer shifts and quadrupole splittings, and ^{57}Fe and ^{55}Mn electron nuclear double resonance (ENDOR) hyperfine coupling constants, are compared with the available experimental data. The Mössbauer and energetic calculations show that the (μ-oxo, μ-hydroxo) models better represent the structure of the Mn(IV)−Fe(III) state than the di-μ-oxo models. The predicted Mn(IV)−Fe(III) distances (2.95 and 2.98 Å) in the (μ-oxo, μ-hydroxo) models are in agreement with the extended X-ray absorption fine structure (EXAFS) experimental value of 2.92 Å (Younker et al. *J. Am. Chem. Soc.* **2008**, *130*, 15022−15027). The effect of the protein and solvent environment on the assignment of the Mn metal position is examined by comparing the relative energies of alternative mono-Mn(II) active site structures. It is proposed that if the Mn(II)−Fe(II) protein is prepared with prior addition of Mn(II) or with Mn(II) richer than Fe(II), Mn is likely positioned at metal site 2, which is further from Phe127.

1. Introduction

Ribonucleotide reductase (RNR) catalyzes the reduction of ribonucleotides to their 2′-deoxyribonucleotide counterparts which are the precursors required in the initial step in DNA biosynthesis.[1,2] Different RNR classes differ in composition and cofactor requirements. However, they display a reaction mechanism with a common theme using metals and free radical chemistry.

The class I RNRs consist of two dissimilar protein subunits, R1 and R2, each a homodimer in an overall $\alpha_2\beta_2$ tetramer. Subunit R1 contains the substrate binding site, and catalyzes the dehydroxylation of the 2′-hydroxyl group of the ribose ring. Subunit R2 contains a binuclear iron cluster. In a conventional class I RNR-R2 from eukaryotes, some prokaryotes and viruses,[3] a tyrosine (Tyr122 in *Escherichia coli*) is found to be close to the diiron center. This tyrosine is crucial since it can bear a radical generated by the R2 diiron cluster. The tyrosine radical functions as a "pilot light" which begins the catalytic reaction by a long-range radical transfer (or proton coupled electron transfer) to generate a thiyl radical on cysteine 439 (in *E. coli*) of subunit R1, which then performs the nucleotide reduction.[4,5] This tyrosine radical has been identified in the oxidized deprotonated form and is stable for days at room temperature.[1] Once this radical is lost, the enzyme becomes inactive. The active form can be regenerated by a complicated sequence of steps involving changes in oxidation state and structural rearrangement with coupled electron and proton transfers. First the resting oxidized diferric met form of R2 is reduced by 2 electrons from a reductase protein to the diferrous form, $R2_{red}$. Next, a molecular oxygen (O_2) binds to the diiron center of $R2_{red}$ and an electron is transferred from Trp48 (in *E. coli*) to one of the iron sites. Afterward, a transient high-oxidation R2 intermediate state, named X, is kinetically and spectroscopically observed. X is evidently the species

*To whom correspondence should be addressed. E-mail: lou@scripps.edu. Fax: 858-7848896.

(1) Wallar, B. J.; Lipscomb, J. D. *Chem. Rev.* **1996**, *96*, 2625–2658.
(2) Sjöberg, B. M. *Struct. Bonding* (*Berlin*) **1997**, *88*, 139–173.
(3) Fontecave, M.; Nordlund, P.; Eklund, H.; Reichard, P. *Adv. Enzymol. Relat. Areas Mol. Biol.* **1992**, *65*, 147–183.
(4) Sturgeon, B. E.; Burdi, D.; Chen, S. X.; Huynh, B. H.; Edmondson, D. E.; Stubbe, J.; Hoffman, B. M. *J. Am. Chem. Soc.* **1996**, *118*, 7551–7557.
(5) Stubbe, J. A.; vanderDonk, W. A. *Chem. Biol.* **1995**, *2*, 793–801.

 Published on Web 07/06/2010

which regenerates the tyrosine radical. RNR-X has captured the attention of many researchers over the past 20 years to elucidate its chemical and structural nature.[4,6−30] A combination of Q-band electron nuclear double resonance (ENDOR) and Mössbauer data on Y122F-R2 indicates the iron centers of X are high spin Fe(III) ($S = 5/2$) and high spin Fe(IV) ($S = 2$) sites that antiferromagnetically couple to give an $S_{total} = 1/2$ ground state.[4]

The radical bearing tyrosine is conserved among more than 200 sequenced R2s, and mutants with a phenylalanine in this position are enzymatically inactive.[31,32] However, an exception was found recently in the RNR-R2 from the pathogenic bacteria *Chlamydia trachomatis* (*Ct*), where a phenylalanine (Phe127) resides in place of the tyrosine residue which bears the radical in conventional RNRs.[33] Further this sequence is similar to that in a number of other pathogenic bacteria.[33] The X-ray structure (1SYY)[33] obtained for *Ct*-R2 contains a Fe(III)−Fe(III) diiron center which is very similar to the diferric center of the hydroxylase component of soluble methane monooxygenase (MMOH). Similar to R2, the reduced diferrous center of MMOH also reacts with O_2. Instead of yielding the intermediate X with Fe(IV)−Fe(III) center, the interaction with O_2 in MMOH yields an Fe(IV)−Fe(IV) intermediate, Q, which can then oxidize methane to methanol.[1,34−37]

Later the Bollinger/Krebs group discovered that the *Ct*-RNR-R2 contains a Mn−Fe center rather than a diiron center in its functional form, and uses the Mn(IV)−Fe(III) cofactor (intermediate X) for radical initiation.[38,39] The high-spin Mn(IV) ($S_{Mn} = 3/2$) antiferromagnetically (AF) couples with the high-spin Fe(III) ($S_{Fe} = 5/2$) to give $S_{total} = 1$. Unlike the conventional RNR, but similar to MMOH, during the reaction between O_2 and the reduced *Ct*-R2, another superoxidized state, Mn(IV)−Fe(IV), was kinetically and spectroscopically observed,[40] in which Mn(IV) ($S_{Mn} = 3/2$) and Fe(IV) ($S_{Fe} = 2$) AF-couple to give $S_{total} = 1/2$. The Mn(IV)−Fe(IV) state then decays by one-electron reduction of the Fe(IV) site to the active form of Mn(IV)−Fe(III). This reduction was found to be mediated by residue Tyr222 which resides on the surface of protein *Ct*-R2.[41]

Currently, a variety of Mössbauer, hyperfine, and EXAFS data are available for the *Ct*-R2 center in different oxidation states.[38,40−44] Roos and Siegbahn have performed B3LYP hybrid density functional theory (DFT) calculations for geometries and energies on *Ct*-R2 active site models which contain the first shell ligands and Phe127.[45] They found the Mn(IV)−Fe(III)−Phe active center to be an equally strong oxidant as the active state in *E. coli* R2 with a tyrosyl radical. Younker et al. also performed DFT calculations on the *Ct*-R2 first-shell ligand models to discover the active-site structure of the Mn(IV)−Fe(III) state.[42] Both theoretical studies proposed that the Mn(IV)−Fe(III) active site contains a terminal water or hydroxo ligand, one bridging μ-oxo, and one bridging μ-hydroxo. However, it is not known which metal site is Mn or Fe, and the detailed structures of the Mn−Fe center in other oxidation states are not well understood. In the calculations by Roos and Siegbahn, the model with Mn(IV) connecting to Glu89 and His123 (site 1, which is closer to Phe127) was predicted to be about 1 kcal mol^{-1} lower in energy than the model with Fe(III) at site 1.[45] However, the stable positions of Mn and Fe centers are probably determined at an early stage of the protein sample preparation. If the Mn(II)−Fe(II) state is prepared by adding first Mn(II) and then Fe(II) to the metal-depleted R2,[38] the Mn and Fe positions resulting from this sequence will likely be locked during the whole activation and catalytic process.

In this paper, we present DFT calculations on large active site quantum cluster models for *Ct*-R2. We first compare the

(6) Bollinger, J. M.; Tong, W. H.; Ravi, N.; Huynh, B. H.; Edmondson, D. E.; Stubbe, J. *J. Am. Chem. Soc.* **1994**, *116*, 8015–8023.
(7) Bollinger, J. M.; Tong, W. H.; Ravi, N.; Huynh, B. H.; Edmondson, D. E.; Stubbe, J. *J. Am. Chem. Soc.* **1994**, *116*, 8024–8032.
(8) Bollinger, J. M., Jr.; Edmondson, D. E.; Huynh, B. H.; Filley, J.; Norton, J. R.; Stubbe, J. *Science* **1991**, *253*, 292–298.
(9) Bollinger, J. M., Jr.; Tong, W. H.; Ravi, N.; Huynh, B. H.; Edmondson, D. E.; Stubbe, J. In *Methods in Enzymology*; Klinman, J. P., Ed.; Academic Press: New York, 1995; p 258.
(10) Bollinger, J. M., Jr.; Stubbe, J.; Huynh, B. H.; Edmondson, D. E. *J. Am. Chem. Soc.* **1991**, *113*, 6289–6291.
(11) Ravi, N.; Bollinger, J. M., Jr.; Huynh, B. H.; Edmondson, D. E.; Stubbe, J. *J. Am. Chem. Soc.* **1994**, *116*, 8007–8014.
(12) Ravi, N.; Bominaar, E. L. *Inorg. Chem.* **1995**, *34*, 1040–1043.
(13) Burdi, D.; Sturgeon, B. E.; Tong, W. H.; Stubbe, J. A.; Hoffman, B. M. *J. Am. Chem. Soc.* **1996**, *118*, 281–282.
(14) Veselov, A.; Scholes, C. P. *Inorg. Chem.* **1996**, *35*, 3702–3705.
(15) Willems, J. P.; Lee, H. I.; Burdi, D.; Doan, P. E.; Stubbe, J.; Hoffman, B. M. *J. Am. Chem. Soc.* **1997**, *119*, 9816–9824.
(16) Riggs-Gelasco, P. J.; Shu, L. J.; Chen, S. X.; Burdi, D.; Huynh, B. H.; Que, L.; Stubbe, J. *J. Am. Chem. Soc.* **1998**, *120*, 849–860.
(17) Burdi, D.; Willems, J.-P.; Riggs-Gelasco, P.; Antholine, W. E.; Stubbe, J.; Hoffman, B. M. *J. Am. Chem. Soc.* **1998**, *120*, 12910–12919.
(18) Shanmugam, M.; Doan, P. E.; Lees, N. S.; Stubbe, J.; Hoffman, B. M. *J. Am. Chem. Soc.* **2009**, *131*, 3370–3376.
(19) Mitić, N.; Saleh, L.; Schenk, G.; Bollinger, J. M. J.; Solomon, E. I. *J. Am. Chem. Soc.* **2003**, *125*, 11200–11201.
(20) Baldwin, J.; Krebs, C.; Ley, B. A.; Edmondson, D. E.; Huynh, B. H.; Bollinger, J. H. *J. Am. Chem. Soc.* **2000**, *122*, 12195–12206.
(21) Krebs, C.; Chen, S. X.; Baldwin, J.; Ley, B. A.; Patel, U.; Edmondson, D. E.; Huynh, B. H.; Bollinger, J. M. *J. Am. Chem. Soc.* **2000**, *122*, 12207–12219.
(22) Siegbahn, P. E. M. *Inorg. Chem.* **1999**, *38*, 2880–2889.
(23) Siegbahn, E. M. *Q. Rev. Biophys.* **2003**, *36*, 91–145.
(24) Han, W.-G.; Lovell, T.; Liu, T.; Noodleman, L. *Inorg. Chem.* **2003**, *42*, 2751–2758.
(25) Han, W.-G.; Lovell, T.; Liu, T.; Noodleman, L. *Inorg. Chem.* **2004**, *43*, 613–621.
(26) Han, W.-G.; Liu, T.; Lovell, T.; Noodleman, L. *J. Am. Chem. Soc.* **2005**, *127*, 15778–15790.
(27) Han, W. G.; Liu, T. Q.; Lovell, T.; Noodleman, L. *Inorg. Chem.* **2006**, *45*, 8533–8542.
(28) Han, W.-G.; Liu, T.; Lovell, T.; Noodleman, L. *J. Inorg. Biochem.* **2006**, *100*, 771–779.
(29) Han, W.-G.; Noodleman, L. *Theor. Chem. Acc.* **2010**, *125*, 305–317.
(30) Han, W.-G.; Noodleman, L. *Dalton Trans.* **2009**, 6045–6057.
(31) Larsson, A.; Sjöberg, B. M. *EMBO J.* **1986**, *5*, 2037–2040.
(32) Pötsch, S.; Lendzian, F.; Ingemarson, R.; Hornberg, A.; Thelander, L.; Lubitz, W.; Lassmann, G.; Graslund, A. *J. Biol. Chem.* **1999**, *274*, 17696–17704.
(33) Högbom, M.; Stenmark, P.; Voevodskaya, N.; McClarty, G.; Graslund, A.; Nordlund, P. *Science* **2004**, *305*, 245–248.
(34) Solomon, E. I.; Brunold, T. C.; Davis, M. I.; Kemsley, J. N.; Lee, S. K.; Lehnert, N.; Neese, F.; Skulan, A. J.; Yang, Y. S.; Zhou, J. *Chem. Rev.* **2000**, *100*, 235–349.
(35) Jin, Y.; Lipscomb, J. D. *J. Biol. Inorg. Chem.* **2001**, *6*, 717–725.
(36) Han, W. G.; Noodleman, L. *Inorg. Chim. Acta* **2008**, *361*, 973–986.
(37) Han, W.-G.; Noodleman, L. *Inorg. Chem.* **2008**, *47*, 2975–2986.
(38) Jiang, W.; Yun, D.; Saleh, L.; Barr, E. W.; Xing, G.; Hoffart, L. M.; Maslak, M. A.; Krebs, C.; Bollinger, J. M. *Science* **2007**, *316*, 1188–1191.
(39) Jiang, W.; Bollinger, J. M.; Krebs, C. *J. Am. Chem. Soc.* **2007**, *129*, 7504–7505.
(40) Jiang, W.; Hoffart, L. M.; Krebs, C.; Bollinger, J. M. *Biochemistry* **2007**, *46*, 8709–8716.
(41) Jiang, W.; Saleh, L.; Barr, E. W.; Xie, J. J.; Gardner, M. M.; Krebs, C.; Bollinger, J. M. *Biochemistry* **2008**, *47*, 8477–8484.
(42) Younker, J. M.; Krest, C. M.; Jiang, W.; Krebs, C.; Bollinger, J. M.; Green, M. T. *J. Am. Chem. Soc.* **2008**, *130*, 15022–15027.
(43) Jiang, W.; Yun, D.; Saleh, L.; Bollinger, J. M.; Krebs, C. *Biochemistry* **2008**, *47*, 13736–13744.
(44) Voevodskaya, N.; Lendzian, F.; Sanganas, O.; Grundmeier, A.; Gräslund, A.; Haumann, M. *J. Biol. Chem.* **2009**, *284*, 4555–4566.
(45) Roos, K.; Siegbahn, P. E. M. *Biochemistry* **2009**, *48*, 1878–1887.

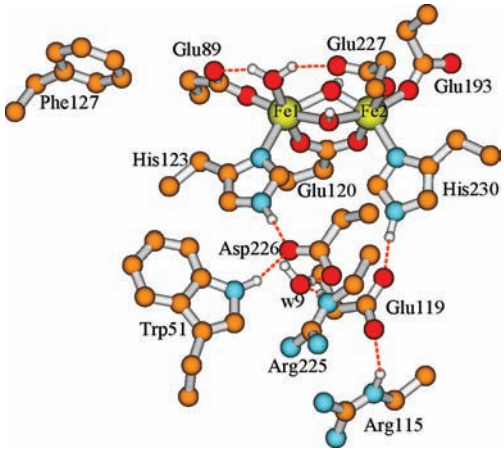

Figure 1. Active site of *Ct*-R2 in the diferric form. Taken from PDB X-ray structure 1SYY.[33] Protons not involved in H-bonds are suppressed for clarity.

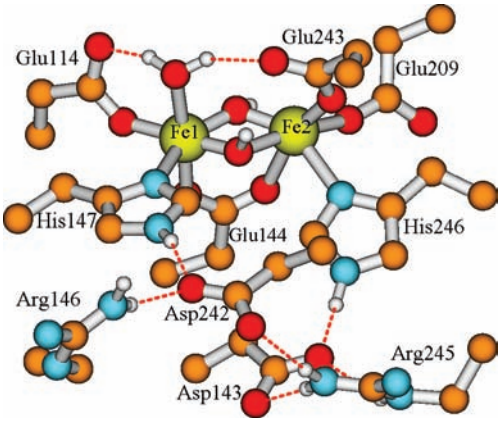

Figure 2. Active site of the diferric MMOH from *Mt* (PDB X-ray structure 1MHY).[50].

relative energies of the Mn1(II)−Fe2(II) (Mn(II) on site 1 and Fe(II) on site 2) and Fe1(II)−Mn2(II) structures. Then deleting Fe(II) from the Mn(II)−Fe(II) models and reoptimizing the structures with only Mn(II) on either site 1 or site 2, we examine without the presence of Fe(II), if there is significant energy preference from the protein and solvent environment for the specific site where Mn(II) will bind. The idea is that if Mn(II) is added to the apo *Ct*-R2 prior to Fe(II) in preparation of the Mn(II)−Fe(II) protein,[39,42,46] it should bind to the site with higher Mn(II)-binding affinity (lower energy). Fe(II), which is added later, would then either bind to the other empty site or replace the Mn(II) in the other site which has lower Mn(II)-binding affinity. As indicated by Jiang et al.,[39,42,46] their best procedure to prepare the Mn(II)−Fe(II) *Ct*-R2 protein involves prior addition of 1.5 equiv of Mn(II) per monomer to apo-R2, and slow addition of 0.75 equiv of Fe(II), to prevent the formation of the inactive form of Fe(II)−Fe(II). Next, by comparing the calculated structures, Mössbauer, and hyperfine properties of the Mn(III)−Fe(III), Mn(IV)−Fe(IV), and Mn(IV)−Fe(III) states in both Mn1−Fe2 and Fe1−Mn2 models, we further examine which models and site placement lead to calculations that most closely reproduce the available experimental data. Because of the similarity of the residues around the metal centers in *E. coli* RNR, *Ct*-RNR, and MMOH, the well studied models for *E. coli* RNR[22,23,26,30] and MMOH[22,36,37,47−49] in different oxidation states become the best candidates for studying similar states of *Ct*-RNR.

2. Comparisons of the Diferric Active Site Structures of *Ct*-R2, *E. coli* R2, and MMOH

In the available X-ray structure (1SYY, resolution 1.7 Å) of *Ct*-R2, the enzyme is in the inactive diiron form.[33] The diiron center and the main H-bonding residues around the center are shown in Figure 1. The first shell ligands include two histidine and four glutamic acid residues, one terminal oxygen species binding to Fe1, and two O(H) bridges. The first shell composition and coordination environment is exactly the same as that found in the diferric center of MMOH from *Methylosinus trichosporium* (*Mt*) OB3b protein (X-ray crystal structure 1MHY, see Figure 2).[50]

Previous studies have shown that the three oxygen species in the MMOH diferric center are one terminal water and two bridging hydroxo ions.[49−53] According to the Fe−O distances observed from the crystal structure, the *Ct*-R2 diferric center should also contain a terminal water and two μ-OH$^-$ bridges as shown in Figure 1. The active site structure of the *Ct*-R2 Mn(III)−Fe(III) state is still unknown. Recent EXAFS experiments on *Ct*-R2 lead to a short Mn(III)−Fe(III) distance of 2.9 Å,[44] which is similar to the Fe(III)−Fe(III) distance in MMOH,[50,54] indicative of the Mn(III)-(μ-OH$^-$)$_2$-Fe(III) center in active form of *Ct*-R2 as well.[44]

The first shell ligands in the diferric center of *E. coli* R2 (Figure 3) are similar to those in *Ct*-R2 (Figure 1). However, in *E.coli* R2, where an aspartic acid (84), rather than a glutamic acid residue binds to Fe1, there is only one bridging oxygen (μ-oxo) in the position between the two histidines, and the other solvent type oxygen between Asp84 and Glu204 is a terminal water binding to Fe2 and H-bonding to both Asp84 and Glu238. In the outer shell H-bonding network, the carboxylate group in Asp237 H-bonds to His118, and a neutral Gln43 side chain H-bonds to both His241 and Asp237. A positively charged Arg236 side chain, which lies on the surface of the protein, indirectly interacts with Asp237 through H-bonding with a water molecule (w727). Also H-bonding to Asp237 is Trp48, which is close to the protein surface and is proposed to be the residue that transfers an electron to the diiron center after O_2 binding when X is formed.

In *Ct*-R2, the H-bonding patterns and residues along the Fe1-His123 direction (His123···Asp226···Trp51(w9···Arg225)) match exactly with those along the Fe1-His118 direction in *E.coli* R2 (His118···Asp237···Trp48(w727···Arg236)). MMOH has the Asp residue in this pattern (Asp242),

(46) Jiang, W.; Xie, J. J.; Norgaard, H.; Bollinger, J. M.; Krebs, C. *Biochemistry* **2008**, *47*, 4477–4483.
(47) Siegbahn, P. E. M.; Blomberg, M. R. A. *Annu. Rev. Phys. Chem.* **1999**, *50*, 221–249.
(48) Gherman, B. F.; Dunietz, B. D.; Whittington, D. A.; Lippard, S. J.; Friesner, R. A. *J. Am. Chem. Soc.* **2001**, *123*, 3836–3837.
(49) Baik, M. H.; Newcomb, M.; Friesner, R. A.; Lippard, S. J. *Chem. Rev.* **2003**, *103*, 2385–2419.
(50) Elango, N.; Radhakrishnan, R.; Froland, W. A.; Wallar, B. J.; Earhart, C. A.; Lipscomb, J. D.; Ohlendorf, D. H. *Protein Sci.* **1997**, *6*, 556–568.
(51) Han, W.-G.; Liu, T. Q.; Lovell, T.; Noodleman, L. *J. Comput. Chem.* **2006**, *27*, 1292–1306.
(52) Lovell, T.; Li, J.; Noodleman, L. *Inorg. Chem.* **2001**, *40*, 5267–5278.
(53) Lovell, T.; Li, J.; Noodleman, L. *Inorg. Chem.* **2001**, *40*, 5251–5266.
(54) Rudd, D. J.; Sazinsky, M. H.; Merkx, M.; Lippard, S. J.; Hedman, B.; Hodgson, K. O. *Inorg. Chem.* **2004**, *43*, 4579–4589.

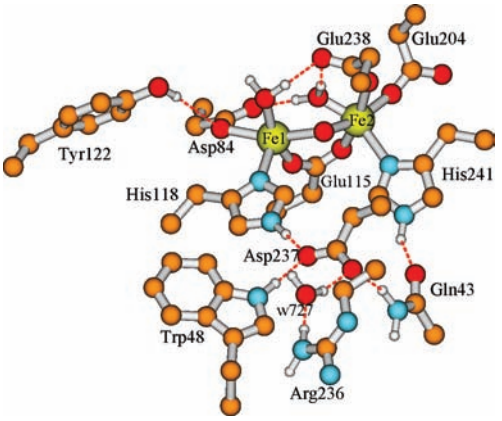

Figure 3. Diferric (met) active site of *E. coli* R2. Taken from X-ray PDB structure 1RIB.[55].

but the positively charged Arg146 is in the position of the tryptophan in RNR-R2 (Trp51 in *Ct* and Trp48 in *E. coli*). Another arginine (Arg245) directly H-bonds to Asp242 in MMOH as well as to the carboxylate group of Asp143. Asp143 then H-bonds to His246. In *Ct*-R2, the carboxylate group of Glu119 is analogous in position and charge to Asp143 in MMOH. There is also another arginine (Arg115) in *Ct*-R2 which H-bonds to Glu119. Therefore, along the Fe2-His230 direction, H-bonding interactions (His230···Glu119···Arg115) in *Ct*-R2 are more like those in MMOH (His246···Asp143···Arg245) than those in *E. coli* RNR.

The active sites of these three proteins share many similarities. Especially for *Ct*-R2 and MMOH, they both have the same kinds of first shell residues, and two negatively charged and two positively charged residues in the second and third shell combined. These similar electrostatic interactions lead to very similar first-shell structures in their diferric state.

To study the active form of *Ct*-R2 active site structures, we will start from the diferric state X-ray structure (Figure 1) and replace one of the Fe sites with Mn. Because of all the structural similarities among the three proteins compared above, the previous structural models for MMOH-Q and *E. coli* RNR-X may also represent the *Ct*-R2Mn(IV)−Fe(IV) and Mn(IV)−Fe(III) active site structures. Some structural rearrangements are needed for the initial geometries of the Mn(II)−Fe(II) state models according to the reduced diferrous *E. coli* R2 and MMOH X-ray crystal structures.[56,57] We will examine these structures by geometry optimization for both Mn1−Fe2 and Fe1−Mn2 alternatives (switching Mn and Fe positions), and using Mössbauer and hyperfine property calculations. The calculated properties will be compared with available experiments.

3. Computational Methodology

3.1. Models. For the Mn(III)−Fe(III) state, the initial positions of the active site side chains and water or hydroxo groups in the model cluster were taken from chain A of the diferric *Ct*-R2 X-ray crystal structure (PDB code: 1SYY) (Figure 1),[33] by breaking the C_β-C_α or C_γ-C_β bonds and adding a linking hydrogen atom to fill the open valence of the terminal carbon atom.[58] The model in which Fe1 is replaced with Mn is denoted as Mn1(III)−Fe2(III), while Fe1(III)−Mn2(III) denotes the model with Fe2 is replaced by Mn. The overall active site model of M1(III)−M2(III) (M1 and M2 represent either Mn or Fe) in the current study is shown in Figure 4. The difference between this structure and the one shown in Figure 1 is that more water molecules observed in the X-ray structure and the side chain of Asn50 are included so as to explicitly represent the H-bonding interactions near the active site. The details of the H-bonding network in the lower part of this cluster, which includes Asp226, Glu119, Arg225, Arg115, and Asn50 side chains, and 11 water (w) molecules, is shown in Figure 5.

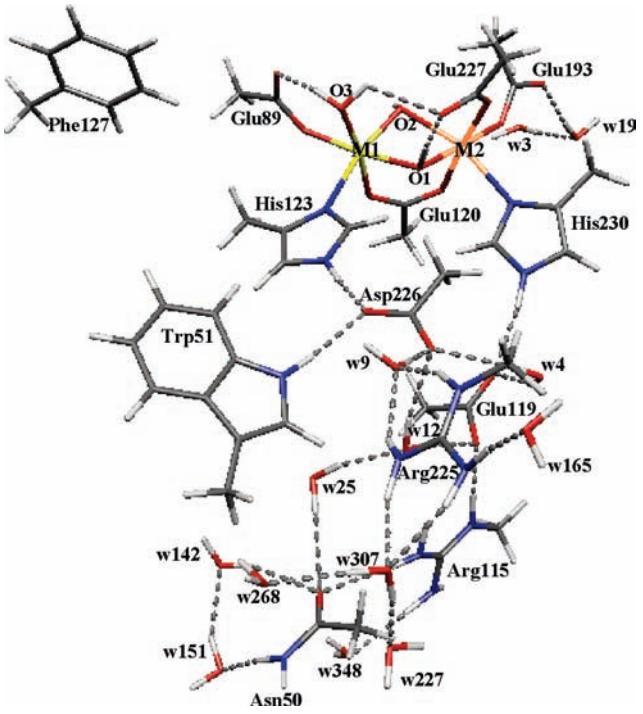

Figure 4. Mn1(III)−Fe2(III) or Fe1(III)−Mn2(III) quantum cluster model of *Ct*-R2 active site in the current study. M1 and M2 represent either Mn or Fe. The details of the H-bonding network in the lower part of this cluster is shown in Figure 5.

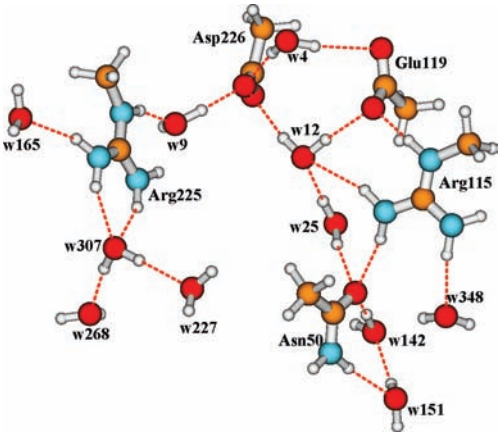

Figure 5. Detailed H-bonding network in the lower part of the active site model in Figure 4, from a different perspective.

(55) Nordlund, P.; Eklund, H. *J. Mol. Biol.* **1993**, *232*, 123–164.
(56) Logan, D. T.; Su, X. D.; Aberg, A.; Regnstrom, K.; Hajdu, J.; Eklund, H.; Nordlund, P. *Structure* **1996**, *4*, 1053–1064.
(57) Rosenzweig, A. C.; Nordlund, P.; Takahara, P. M.; Frederick, C. A.; Lippard, S. J. *Chem. Biol.* **1995**, *2*, 409–418.
(58) Han, W.-G.; Tajkhorshid, E.; Suhai, S. *J. Biomol. Struct. Dyn.* **1999**, *16*, 1019–1032.

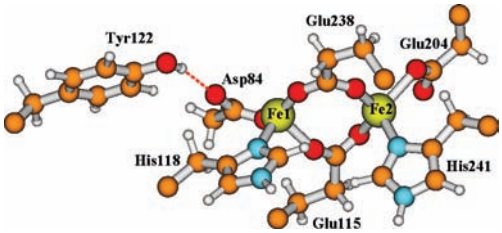

Figure 6. Active site structure of reduced diferrous state of *E. coli* R2.[56].

On the basis of theoretical/computational DFT models and spectroscopic evidence (optical, EPR/ENDOR, and Mössbauer), the currently proposed MMOH-Q in Fe(IV)−Fe(IV) state and *E. coli* RNR-X (class Ia) in Fe(III)−Fe(IV) state have very similar first shell structures as shown in Figure 2 (and also in Figures 1 and 4), but with a di-μ-oxo center (for Q and X) or with one μ-oxo and one μ-hydroxo bridge (for X), rather than the di-μ-hydroxo bridge seen in the *Ct*-R2 Fe(III)−Fe(III) structure.[30,36,37,48,49,59] Therefore, our *Ct*-R2Mn(IV)−Fe(IV) state active site model is constructed from the Mn(III)−Fe(III) structure by deleting both "H" protons from the di-μ-hydroxo bridge shown in Figure 4. Such a di-μ-oxo structure will also be studied for the Mn(IV)−Fe(III) state, and be compared with another Mn(IV)−Fe(III) structure with the (μ-oxo, μ-hydroxo) center.

Currently no X-ray crystal structure has been obtained for either the Mn(II)−Fe(II) or the Fe(II)−Fe(II) state of *Ct*-R2. One observed structural result is the long Mn(II)−Fe(II) distance of 4.15 Å reported from EXAFS experiments.[44] However, the samples used in these experiments were mixtures of different oxidation states, which makes the evaluation of structures for specific oxidation states difficult. Also, because of inelastic scattering, long metal−metal distances are hard to determine accurately by EXAFS. The Fe(II)−Fe(II) distances in diferrous state X-ray crystal structures are 3.94 Å for *E. coli* R2 and 3.28 Å for MMOH.[56,57] The ligand pattern in the reduced state of the *E. coli* R2 active site (Figure 6) differs from that of the diferric state (Figure 3) in that the carboxylate groups of both Glu115 and Glu238 are in a bidentate binding mode, there are no bridging or terminally bound oxygen species, and both Fe1 and Fe2 have coordination number 4. In the reduced MMOH active site (Figure 7), the carboxylate group of Glu243 changes to the monodentate bridging position. This differs both from the diferrous structure of *E. coli* RNR, and from diferric MMOH. Two water molecules are coordinated to Fe1. However, the water which H-bonds to Glu114 only weakly interacts with Fe1 (with long O−Fe1 distance of 2.63 Å).

The reduced state of *Ct*-R2 may have a closely related active site structure to either the diferrous *E. coli* R2 or MMOH. We will therefore study the two forms of Mn(II)−Fe(II) models by deleting O1, deleting or changing O2 to a terminal water, and changing the orientation of Glu227 in the Mn(III)−Fe(III) (Figure 4) model according to the relative positions of Glu238 and Glu243 in reduced *E. coli* R2 and MMOH (Figures 6 and 7), respectively. Again, both the Mn1(II)−Fe2(II) and Fe1(II)−Mn2(II) forms will be studied to compare their relative energies. The models constructed according to the active site structures of reduced *E. coli* R2 and MMOH will be denoted [Mn1(II)−Fe2(II)-E and Fe1(II)−Mn2(II)-E] and [Mn1(II)−Fe2(II)-M and Fe1(II)−Mn2(II)-M], respectively (Figure 8).

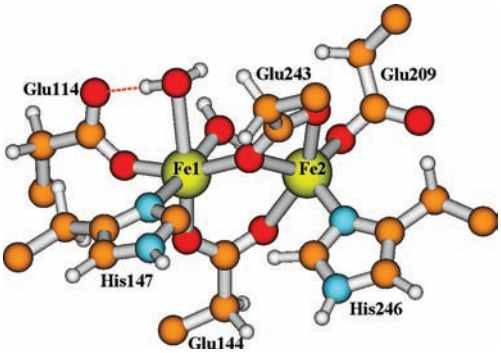

Figure 7. Active site structure of reduced diferrous MMOH.[57].

3.2. DFT Calculations. All density functional spin-unrestricted calculations have been performed using the Amsterdam Density Functional (ADF) packages.[60−63] For a simplified representation of the stabilizing effects of the protein and solvent which generate a polar environment, the geometries of the model clusters were optimized using the COSMO (conductor-like screening model) solvation model in ADF.[64−67] The COSMO model is a dielectric solvent continuum model in which the solute molecule is embedded in a molecular shaped cavity surrounded by a dielectric medium with a given dielectric constant. Our recent studies show that certain calculated Fe-ligand distances are significantly influenced by the size of the quantum cluster and the dielectric constant ε chosen for the COSMO solvation calculations.[29] However, for large quantum cluster models which include the main polar groups up to the fourth coordination shells of the residues from the iron centers, changing the dielectric constant (ε) in COSMO in the range of [4, 20] changes the main Fe-ligand distances, Mössbauer, and hyperfine properties very little.[30] On the other hand, the relative energies and thus the pK_a's predicted by the COSMO calculations are highly dependent on the dielectric constants. Choosing the dielectric constant to best predict the pK_a's is system and site dependent.[30] In our current study, we will calculate the acidity of the bridging oxygen (site O2, in the position between Glu89 and Glu193) in the Mn(IV)−Fe(III) state. Our recent *E. coli* RNR-X studies[30] show that $\varepsilon = 4$ in COSMO is the best for large quantum models in reproducing the pK_a value of site O2 obtained from the Poisson−Boltzmann self-consistent reaction field (PB-SCRF)[30,68−76] calculations which include both the protein field and the

(59) Mitić, N.; Clay, M. D.; Saleh, L.; Bollinger, J. M. J.; Solomon, E. I. *J. Am. Chem. Soc.* **2007**, *129*, 9049–9065.
(60) *ADF2007.01*; SCM, Theoretical Chemistry, Vrije Universiteit: Amsterdam, The Netherlands; http://www.scm.com.
(61) te Velde, G.; Bickelhaupt, F. M.; Baerends, E. J.; Guerra, C. F.; Van Gisbergen, S. J. A.; Snijders, J. G.; Ziegler, T. *J. Comput. Chem.* **2001**, *22*, 931–967.
(62) Giammona, D. A.; Bashford, D.; Han, W.-G.; Noodleman, L. *The developmental version of ADF2009.01, with implementation of the Poisson-Boltzmann self-consistent reaction field methodology*, 2010.
(63) *ADF2009.01*; SCM, Theoretical Chemistry, Vrije Universiteit: Amsterdam, The Netherlands; http://www.scm.com.
(64) Klamt, A.; Schüürmann, G. *J. Chem. Soc., Perkin Trans. II* **1993**, 799–805.
(65) Klamt, A. *J. Phys. Chem.* **1995**, *99*, 2224–2235.
(66) Klamt, A.; Jonas, V. *J. Chem. Phys.* **1996**, *105*, 9972–9981.
(67) Pye, C. C.; Ziegler, T. *Theor. Chem. Acc.* **1999**, *101*, 396–408.
(68) Chen, J. L.; Noodleman, L.; Case, D. A.; Bashford, D. *J. Phys. Chem.* **1994**, *98*, 11059–11068.
(69) Bashford, D. An Object-Oriented Programming Suite for Electrostatic Effects in Biological Molecules. In *Scientific Computing in Object-Oriented Parallel Environments* (*Lecture Notes in Computer Science*); Ishikawa, Y., Oldehoeft, R. R., Reynders, J. V. W., Tholburn, M., Eds.; Springer: Berlin, 1997; Vol. *1343*, pp 233−240.
(70) Li, J.; Nelson, M. R.; Peng, C. Y.; Bashford, D.; Noodleman, L. *J. Phys. Chem. A* **1998**, *102*, 6311–6324.
(71) Liu, T.; Han, W.-G.; Himo, F.; Ullmann, G. M.; Bashford, D.; Toutchkine, A.; Hahn, K. M.; Noodleman, L. *J. Phys. Chem. A* **2004**, *108*, 3545–3555.
(72) Han, W.-G.; Liu, T.; Himo, F.; Toutchkine, A.; Bashford, D.; Hahn, K. M.; Noodleman, L. *ChemPhysChem* **2003**, *4*, 1084–1094.
(73) Toutchkine, A.; Han, W.-G.; Ullmann, M.; Liu, T. Q.; Bashford, D.; Noodleman, L.; Hahn, K. M. *J. Phys. Chem. A* **2007**, *111*, 10849–10860.
(74) Asthagiri, D.; Dillet, V.; Liu, T. Q.; Noodleman, L.; Van Etten, R. L.; Bashford, D. *J. Am. Chem. Soc.* **2002**, *124*, 10225–10235.
(75) Asthagiri, D.; Liu, T. Q.; Noodleman, L.; Van Etten, R. L.; Bashfordt, D. *J. Am. Chem. Soc.* **2004**, *126*, 12677–12684.
(76) Thompson, M. J.; Bashford, D.; Noodleman, L.; Getzoff, E. D. *J. Am. Chem. Soc.* **2003**, *125*, 8186–8194.

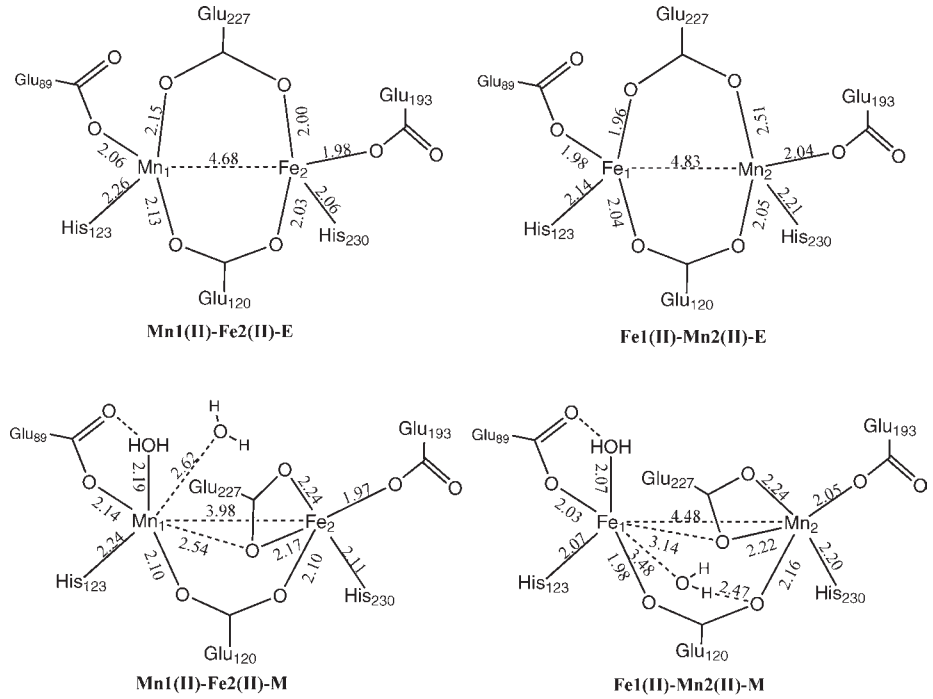

Figure 8. Mn−Fe and main metal−ligand distances in the DFT(OPBE) optimized *Ct*-R2 Mn1(II)−Fe2(II)-E, Fe1(II)−Mn2(II)-E, Mn1(II)−Fe2(II)-M, and Fe1(II)−Mn2(II)-M model structures (the endings E and M refer to the models constructed according to the reduced diferrous active site structures of *E.coli* R2 (Figure 6) and MMOH (Figure 7), respectively). The residues in the outer shells of the active site models are shown in Figures 4 and 5.

reaction fields. Therefore, we will use $\varepsilon = 4$ in the Mn(II)−Fe(II), Mn(III)−Fe(III), Mn(IV)−Fe(IV), and Mn(IV)−Fe(III) state large model COSMO calculations. The van der Waals radii for atoms Fe, C, O, N, and H are taken as 1.5, 1.7, 1.4, 1.55, and 1.2 Å, respectively. The probe radius for the contact surface between the cluster and solvent was set to 2.0 Å.

In all calculations, the parametrization of Vosko, Wilk, and Nusair (VWN)[27] was used for the local density approximation term, and the OPBE[77−79] functional is used for the nonlocal exchange and correlation terms. OPBE is the combination of Handy's optimized exchange (OPTX)[79] and PBE correlation (PBEc) functionals.[77,78] This potential correctly predicts the spin states for several iron complexes.[80−82] We have applied this potential in our *E. coli* RNR-X and MMOH intermediates Q and P studies, and compared the results with our previous PW91[83] calculations.[29,30,36,37] Triple-ζ polarization (TZP) Slater-type basis sets with frozen cores (C(1s), N(1s), O(1s), and Fe-(1s,2s,2p) are frozen) are applied for geometry optimizations. The linking H atoms on the outer shell residue fragments Phe127, Trp51, Asp226, Glu119, Arg225, Arg115, and Asn50 are fixed during the geometry optimizations.

Mössbauer parameter and hyperfine A-tensor calculations were then performed on the optimized geometries using TZP basis set for all atoms without freezing the core electrons. The accuracy parameter for the numerical integration grid was set to 4.0.

Usually the AF spin-coupled state cannot be obtained directly from the normal DFT calculations in ADF. As in previous work, we represent the AF spin-coupled state in DFT by a "broken-symmetry" (BS) state,[84−86] where a spin-unrestricted determinant is constructed in which the Fe site has spin-up electrons as majority spin and the Mn site has spin-down electrons. To obtain this broken-symmetry solution, first we construct a ferromagnetically (F) spin-coupled determinant, where the spins on both Fe and Mn are aligned in a parallel fashion. Then we rotate the spin vector located on the Mn site by interchanging the α and β fit density blocks on Mn from the output file TAPE21 created by this F-coupled calculation in ADF. Using the modified TAPE21 as a restart file and reading the starting spin density from there, we then obtain the expected BS state through single-point energy calculation or geometry optimization.

The BS state obtained from DFT calculations is a mixture of pure spin states. When the following Heisenberg Hamiltonian H (with Heisenberg coupling J) is applicable,

$$H = -2J\boldsymbol{S}_1\cdot\boldsymbol{S}_2 \tag{1}$$

the energy difference between the F-coupling ($S_{\text{total}} = S_{\max} = S_1 + S_2$) and the BS ($S_{\text{total}} = S_{\min} = |S_1 - S_2|$) states can be described by

$$\begin{aligned} E_{\text{F}} - E_{\text{BS}} &= -4JS_1S_2 \\ &(= -20J \text{ for Mn(II)−Fe(II) and Mn(III)−Fe(III) states}) \\ &(= -12J \text{ for Mn(IV)−Fe(IV) state}) \\ &(= -15J \text{ for Mn(IV)−Fe(III) state}) \end{aligned} \tag{2}$$

(Note that for a completely delocalized-mixed valence dimer, a more general spin Hamiltonian is $H = -2J_0\boldsymbol{S_1}\cdot\boldsymbol{S_2} \pm B(S_{\text{total}} + 1/2)$,

(77) Perdew, J. P.; Burke, K.; Ernzerhof, M. *Phys. Rev. Lett.* **1996**, *77*, 3865–3868.
(78) Perdew, J. P.; Burke, K.; Ernzerhof, M. *Phys. Rev. Lett.* **1997**, *78*, 1396–1396.
(79) Handy, N. C.; Cohen, A. J. *Mol. Phys.* **2001**, *99*, 403–412.
(80) Swart, M.; Groenhof, A. R.; Ehlers, A. W.; Lammertsma, K. *J. Phy. Chem. A* **2004**, *108*, 5479–5483.
(81) Swart, M.; Ehlers, A. W.; Lammertsma, K. *Mol. Phys.* **2004**, *102*, 2467–2474.
(82) Swart, M. *J. Chem. Theory Comput.* **2008**, *4*, 2057–2066.
(83) Perdew, J. P.; Chevary, J. A.; Vosko, S. H.; Jackson, K. A.; Pederson, M. R.; Singh, D. J.; Fiolhais, C. *Phys. Rev. B* **1992**, *46*, 6671–6687.
(84) Noodleman, L. *J. Chem. Phys.* **1981**, *74*, 5737–5743.
(85) Noodleman, L.; Case, D. A. *Adv. Inorg. Chem.* **1992**, *38*, 423–470.
(86) Noodleman, L.; Lovell, T.; Han, W.-G.; Liu, T.; Torres, R. A.; Himo, F. Density Functional Theory. In *Comprehensive Coordination Chemistry II, From Biology to Nanotechnology*; Lever, A. B., Ed.; Elsevier Ltd: Amsterdam, 2003; Vol. *2*, pp 491−510.

where B is the resonance delocalization parameter.[87,88] If the total spin S_{total} is small and B is not large, the resonance stabilization energy $-B(S_{total} + 1/2)$ is often neglected. In this case, this term is largely quenched by vibronic effects or other environmental effects, including solvation, and it is reduced by the intrinsic site inequivalence between Mn and Fe.) J is then obtained from eq 2, and the pure-spin ground state energy E_0 for the particular spin state (S_1, S_2) coupled to S_{min} according to the broken-symmetry geometry is estimated as:

$$\begin{aligned} E_0 &= E_F + JS_{max}(S_{max} + 1) - JS_{min}(S_{min} + 1) \\ &(= E_F + 24J \text{ for Mn(II)}-\text{Fe(II) and Mn(III)}-\text{Fe(III) states}) \\ &(= E_F + 15J \text{for Mn(IV)}-\text{Fe(IV) state}) \\ &(= E_F + 18J \text{ for Mn(IV)}-\text{Fe(III) state}) \end{aligned} \quad (3)$$

For more accurate calculations, both BS and F-coupled high-spin state geometries need to be optimized. The structure with the minimum E_0 can be obtained by extrapolating the geometries between the optimized BS and F-coupled geometries. For current *Ct*-R2 models, since the J coupling constant is small, the Mn−Fe centers are weakly coupled, and the BS and F-coupled states do not differ much. For simplicity, the model geometries are only optimized at the BS state, and an F-coupled high-spin single-point energy calculation is performed at the BS optimized geometry to get the E_F energy. The J and E_0 values are then calculated from eqs 2 and 3.

3.2. Mössbauer Isomer Shift and Quadrupole Splitting Calculations. These properties require all-electron (i.e., without frozen core approximation) calculations. After geometry optimization, a high-spin F-coupled single-point energy calculation (in COSMO) with all-electron TZP Slater-type basis sets is performed at the BS optimized geometry, and the energy E_F is obtained. Its TAPE21 file fit density section is then modified by interchanging the α and β fit density blocks on the Mn site. Starting from the modified TAPE21, a BS state single-point energy calculation in COSMO again with all-electron TZP Slater-type basis sets is then performed to obtain the electron density ($\rho(0)$) and the electric field gradient (EFG) at the Fe nucleus, the hyperfine A-tensors, and the BS state energy E_{BS}.

The Mössbauer isomer shifts δ are calculated based on $\rho(0)$:

$$\delta = \alpha(\rho(0) - A) + C \quad (4)$$

In our previous studies,[36,51] the parameters α and C have been fitted separately for the $Fe^{2+,2.5+}$ and $Fe^{2.5+,3+,3.5+,4+}$ complexes for PW91, OPBE, and OLYP, with all-electron TZP Slater type basis sets. For the $Fe^{2.5+,3+,3.5+,4+}$ complexes, we have obtained $A = 11877.0$, $\alpha = -0.312$, and $C = 0.373$ mm s^{-1} for OPBE potential.

For calculating the Mössbauer quadrupole splittings (ΔE_Q), the EFG tensors V are diagonalized, and the eigenvalues are reordered so that $|V_{zz}| \geq |V_{yy}| \geq |V_{xx}|$. The asymmetry parameter η is defined as

$$\eta = (V_{xx} - V_{yy})/V_{zz} \quad (5)$$

Then the ΔE_Q for ^{57}Fe of the nuclear excited state ($I = 3/2$) can be calculated as

$$\Delta E_Q = 1/2eQV_{zz}(1+\eta^2/3)^{(1/2)} \quad (6)$$

where e is the electrical charge of a positive electron, Q is the nuclear quadrupole moment (0.15 barns) of Fe.[89]

3.3. Hyperfine A-Tensor Calculations. The ^{57}Fe and ^{55}Mn hyperfine coupling constants are predicted based on the A-tensor calculations in ADF (the spin−orbit coupling contributions to the A-tensors are neglected), which accounts for only the total (net) number of unpaired electrons ($n_\alpha - n_\beta$) in the system. This algorithm acts as if we had a simple uncoupled system of spin S_{total}. For the present systems with high spin AF coupled sites, we need to rescale the ADF-obtained A-tensors by the spin projection coupling factors $|K_i S_{total}/S_i|$ (i = Fe or Mn).

In different Mn−Fe states, according to[90]

$$K_{Fe} + K_{Mn} = 1 \quad (7)$$

and

$$K_i = \langle \boldsymbol{S}_i \cdot \boldsymbol{S}_{total} \rangle / \langle \boldsymbol{S}_{total} \cdot \boldsymbol{S}_{total} \rangle \quad (8)$$

one can deduce that, for *Ct*-R2 in the Mn(III)−Fe(III) state, we have ($K_{Fe} = 7/3$, $S_{Fe} = 5/2$, $S_{total} = 1/2$) for Fe(III) site, and ($K_{Mn} = -4/3$, $S_{Mn} = 2$, $S_{total} = 1/2$) for Mn(III).[25,26,91,92] For the cluster in the Mn(IV)−Fe(IV) state, we have ($K_{Fe} = 2$, $S_{Fe} = 2$, $S_{total} = 1/2$) for Fe(IV) site, and ($K_{Mn} = -1$, $S_{Mn} = 3/2$, $S_{total} = 1/2$) for Mn(IV). For the Mn(IV)−Fe(III) state, we have ($K_{Fe} = 7/4$, $S_{Fe} = 5/2$, $S_{total} = 1$) for Fe(III), and ($K_{Mn} = -3/4$, $S_{Mn} = 3/2$, $S_{total} = 1$) for Mn(IV). Absolute values of the coupling factors will be used, since the broken symmetry state carries the proper A-tensor sign.

3.4. pK_a Calculations. Debate still exists over whether the *E. coli* RNR-X diiron center contains two μ-oxo bridges $(\mu\text{-O})_2$ or one bridging oxo and one bridging hydroxo (μ-O)(μ-OH^-). In this paper we will study which of the two forms is energetically more favored for the *Ct*-R2 Mn(IV)−Fe(III) state. This requires calculation of the pK_a value for the bridging site O2 (see Figure 4, the bridging oxygen site positioned between Glu89 and Glu193) with O1 deprotonated.

In general, for the following process (M represents "Model"),

$$\text{M(protonated)} \rightarrow \text{M(non-protonated)} + H^+ \quad (9)$$

the pK_a value for the protonated group can be calculated by

$$\begin{aligned} 1.37\text{p}K_a = {} & E_0[\text{M(non-protonated)}] - E_0[\text{M(protonated)}] \\ & + E(H^+) + \Delta G_{sol}(H^+, 1\text{atm}) - T\Delta S_{gas}(H^+) + \Delta\text{ZPE} \\ & + 5/2RT \end{aligned} \quad (10)$$

For calculating the pK_a of site O2, E_0[M(nonprotonated)] and E_0[M(protonated)] represent the energies (including COSMO solvation) of the Mn(IV)-$(\mu\text{-O})_2$−Fe(III) and Mn(IV)-(μ-O)-(μ-OH^-)−Fe(III) models, respectively. The final spin projected energies (E_0) obtained from the all-electron TZP single-point energy high-spin and broken-symmetry calculations are used here. $E(H^+) = 12.6416$ eV is the calculated energy of a proton with respect to a spin restricted hydrogen atom obtained from gas-phase OPBE calculation. $\Delta G_{sol}(H^+, 1\text{ atm})$ is the solvation free energy of a proton at 1 atm pressure. We will use −263.98 kcal mol^{-1} [30,93−95] for this term since so far it is the best measured value (previously we have used −262.11 kcal mol^{-1} which was obtained from experimental

(87) Mouesca, J. M.; Chen, J. L.; Noodleman, L.; Bashford, D.; Case, D. A. *J. Am. Chem. Soc.* **1994**, *116*, 11898–11914.
(88) Zhao, X. G.; Richardson, W. H.; Chen, J. L.; Li, J.; Noodleman, L.; Tsai, H. L.; Hendrickson, D. N. *Inorg. Chem.* **1997**, *36*, 1198–1217.
(89) Martinez-Pinedo, G.; Schwerdtfeger, P.; Caurier, E.; Langanke, K.; Nazarewicz, W.; Sohnel, T. *Phys. Rev. Lett.* **2001**, *87*, 062701(1−4).
(90) Pelmenschikov, V.; Case, D. A.; Noodleman, L. *Inorg. Chem.* **2008**, *47*, 6162–6172.
(91) Noodleman, L.; Chen, J. L.; Case, D. A.; Giori, C.; Rius, G.; Mouesca, J. M.; Lamotte, B. Isotropic Proton Hyperfine Coupling in High Potential $[Fe_4S_4]^{3+}$ Models. In *Nuclear Magnetic Resonance of Paramagnetic Macromolecules*; La Mar, G. N., Ed.; Kluwer Academic Publishers: The Netherlands, 1995; pp 339−367.
(92) Sinnecker, S.; Neese, F.; Noodleman, L.; Lubitz, W. *J. Am. Chem. Soc.* **2004**, *126*, 2613–2622.
(93) Tissandier, M. D.; Cowen, K. A.; Feng, W. Y.; Gundlach, E.; Cohen, M. H.; Earhart, A. D.; Coe, J. V.; Tuttle, T. R. *J. Phys. Chem. A* **1998**, *102*, 7787–7794.
(94) Lewis, A.; Bumpus, J. A.; Truhlar, D. G.; Cramer, C. J. *J. Chem. Educ.* **2004**, *81*, 596–604.
(95) Lewis, A.; Bumpus, J. A.; Truhlar, D. G.; Cramer, C. J. *J. Chem. Educ.* **2007**, *84*, 934.

and theoretical analysis[26]). The translational entropy contribution to the gas-phase free energy of a proton is taken as $-T\Delta S_{gas}(H^+) = -7.76$ kcal mol^{-1} at 298 K and 1 atm pressure.[96] The zero point energy difference term ΔZPE is estimated as -7.29 kcal mol^{-1} taken from previous frequency calculations for small *E. coli* RNR-X models.[30]

3.5. Finite-Difference Poisson−Boltzmann Self-Consistent Reaction Field (PB-SCRF) Calculations. The PB-SCRF[30,62,68−76] calculations are applied only in section 4.2, to see if the protein and solvent environment shows any preference between the two metal binding sites for Mn(II) binding when Fe(II) is absent.

Three dielectric regions are defined in the PB-SCRF calculations: the quantum cluster region ($\varepsilon = 1$), the protein region ($\varepsilon = 4$), and the solvent (water) region ($\varepsilon = 80$). The diferric *Ct*-R2 X-ray crystal structure (1SYY)[33] is used for the geometry of the protein environment. The PARSE[97] atomic radii and charges are assigned to atoms in the protein which generate the protein field. During PB-SCRF, the active site model is computed by DFT calculation in the presence of the protein field and reaction field. The protein field acts as a fixed potential. The reaction field is evaluated from a finite-difference solution to the Poisson−Boltzmann (PB) equation, and self-consistency between the reaction field and the electronic structure of the quantum cluster is achieved by iteration.

The DFT/PB-SCRF procedure is described briefly as follows. (**1**) A gas-phase DFT single-point energy calculation is performed at the COSMO-optimized geometry. (**2**) The CHELPG algorithm[98] combined with singular value decomposition[87] is then used to fit the point charges of each atom (charges for the linking H atoms are set to zero) from the molecular electrostatic potentials (ESP) calculated by ADF. (**3**) The interaction energy of the active site ($\varepsilon = 1$) with the protein ($\varepsilon = 4$) and solvent ($\varepsilon = 80$) environment is estimated by solving the Poisson−Boltzmann equation using the MEAD (Macroscopic Electrostatics with Atomic Detail) program developed by Bashford.[99−102] (**4**) The reaction field plus protein field potential obtained from step **3** is then added to the Hamiltonian of the DFT single-point energy calculation. The iteration of **1**−**4** continues until self-consistency between the reaction field potential and the electronic structure of solute is achieved. This DFT/PB-SCRF procedure has been recently implemented into a developmental version of ADF2009 following up on our work using earlier ADF program versions.[30,62,63,68−76]

4. Results and Discussion

4.1. Mn(II)−Fe(II) state: Mn1(II)−Fe2(II)-E, Fe1(II)−Mn2(II)-E, Mn1(II)−Fe2(II)-M, and Fe1(II)−Mn2(II)-M. As mentioned above, four Mn(II)−Fe(II) *Ct*-R2 active site models are studied here. The initial geometries of Mn1(II)−Fe2(II)-E and Fe1(II)−Mn2(II)-E are constructed according to the Fe(II)−Fe(II) active site structure of *E. coli* R2 (Figure 6), and Mn1(II)−Fe2(II)-M and Fe1(II)−Mn2(II)-M are established based on the Fe(II)−Fe(II) structure of MMOH (Figure 7).

All the model geometries are optimized within COSMO solvation model. Our previous studies on the reduced diferrous active sites of *E. coli* R2 and MMOH show very similar structural, energetic, and Mössbauer properties for F- and AF-coupled Fe(II)−Fe(II) spin states.[51] To be consistent with the calculations in other states, here we will only present the AF-coupled calculations for the Mn(II)−Fe(II) state. The main bond lengths around the metal centers at the optimized geometries are given in Figure 8. Other calculated properties including the Mössbauer isomer shifts (δ) and quadrupole splittings (ΔE_Q), net spin populations (NSP), Heisenberg J coupling constants, and spin projected energies are given in Table 1. The very small J coupling constants calculated for the four models do show the similar energies of the F- and AF-coupled reduced *Ct*-R2 states.

The net spin populations are the main indication of the high-spin or intermediate-spin character of the metal sites. In the ideal ionic limit, the net unpaired spin populations are 5 and 4 for the high-spin Mn(II) (five d-electrons) and Fe(II) (six d-electrons) sites, respectively. The absolute calculated net spins from Mulliken population analysis given in Table 1 for the four model clusters are very close to the ionic limit, indicative of the high-spin Mn(II) and Fe(II) solutions. The opposite signs for the spin densities just indicate the AF-coupling.

The OPBE potential predicts very long Mn(II)−Fe(II) distances (Figure 8) for the Mn1(II)−Fe2(II)-E and Fe1(II)−Mn2(II)-E models. The Mn(II)−Fe(II) distances predicted for the Mn1(II)−Fe2(II)-M and Fe1(II)−Mn2(II)-M models are shorter and closer to the 4.15 Å reported from EXAFS experiment. Since the first-shell ligand components and the diferric state structures are similar for *Ct*-R2 and MMOH active sites, it is more likely that the first-shell ligand structure of reduced state *Ct*-R2 is also similar to the diferrous center of MMOH. During geometry optimization in both Mn1(II)−Fe2(II)-M and Fe1(II)−Mn2(II)-M, as the Mn(II)−Fe(II) distance elongates, the monobridging oxygen atom of the Glu227 side chain and one of the terminal water molecules move away from site 1. In Mn1(II)−Fe2(II)-M these O−Mn1 distances are 2.54 (for O-Glu227) and 2.62 (for H_2O) Å. In Fe1(II)−Mn2(II)-M both of these are even further from Fe1, and the water molecule H-bonds with one of the oxygen atoms of the Glu120 side chain with 2.47 Å (O···O distance). Therefore, this water molecule may not be present in the active site. We note also that for every coordination site in Figure 8, Fe(II) displays shorter bond lengths to ligands than Mn(II) in the same site. Also the highest coordination number for Mn(II) is 5 in Fe1(II)−Mn2(II)-M (not counting long Mn(II)-ligand bonds > 2.5 Å).

No ^{57}Fe Mössbauer experiments are available for the reduced *Ct*-R2 state. The calculated Mössbauer isomer shifts (Table 1) are almost the same for the four models and close to the experimental data of 1.26 and 1.3 mm s^{-1} observed for reduced *E. coli R2* and MMOH, respectively.[103−105] When Fe is at site 1, its calculated quadrupole splitting value is about 0.5 mm s^{-1} smaller than the

(96) Tawa, G. J.; Topol, I. A.; Burt, S. K.; Caldwell, R. A.; Rashin, A. A. *J. Chem. Phys.* **1998**, *109*, 4852–4863.
(97) Sitkoff, D.; Sharp, K. A.; Honig, B. *J. Phys. Chem.* **1994**, *98*, 1978–1988.
(98) Breneman, C. M.; Wiberg, K. B. *J. Comput. Chem.* **1990**, *11*, 361–373.
(99) Bashford, D. *Curr. Opin. Struct. Biol.* **1991**, *1*, 175–184.
(100) Bashford, D.; Gerwert, K. *J. Mol. Biol.* **1992**, *224*, 473–486.
(101) Lim, C.; Bashford, D.; Karplus, M. *J. Phys. Chem.* **1991**, *95*, 5610–5620.
(102) Bashford, D.; Case, D. A.; Dalvit, C.; Tennant, L.; Wright, P. E. *Biochemistry* **1993**, *32*, 8045–8056.
(103) Lynch, J. B.; Juarez-Garcia, C.; Münck, E.; Que, L., Jr. *J. Biol. Chem.* **1989**, *264*, 8091–8096.
(104) Fox, B. G.; Hendrich, M. P.; Surerus, K. K.; Andersson, K. K.; Froland, W. A.; Lipscomb, J. D.; Munck, E. *J. Am. Chem. Soc.* **1993**, *115*, 3688–3701.
(105) Liu, K. E.; Valentine, A. M.; Wang, D. L.; Huynh, B. H.; Edmondson, D. E.; Salifoglou, A.; Lippard, S. J. *J. Am. Chem. Soc.* **1995**, *117*, 10174–10185.

Table 1. Calculated Fe Mössbauer Isomer Shifts (δ, mm s^{-1}), Quadrupole Splittings (ΔE_Q, mm s^{-1}), η, Net Spin Populations (NSP), J Coupling Constants (cm^{-1}), and Spin Projected Energies (E_0, eV) for the Active Site Models of Mn1(II)−Fe2(II)-E, Fe1(II)−Mn2(II)-E, Mn1(II)−Fe2(II)-M, and Fe1(II)−Mn2(II)-M[a]

	Mn1(II)−Fe2(II)-E	Fe1(II)−Mn2(II)-E	Mn1(II)−Fe2(II)-M	Fe1(II)−Mn2(II)-M
δ(Fe)	1.15	1.13	1.15	1.10
ΔE_Q(Fe)	3.00	2.48	3.13	2.50
η	0.53	0.37	0.15	0.70
NSP(Mn)	−5.02	−4.92	−4.97	−4.93
NSP(Fe)	3.80	3.81	3.81	3.82
J	−3	−1	0.1	−2
E_0	−1043.9741	−1043.9576	−1072.9992	−1073.0718

[a] The endings E and M refer to the models constructed according to the reduced state active site structures of *E.coli* R2 and MMOH, respectively.

value with Fe at site 2. This may help us to distinguish the metal sites once experimental Mössbauer data are available for the reduced *Ct*-R2 state.

The relative energies are a potentially important indicator whether Mn1−Fe2 or Fe1−Mn2 metal setting is favored. However, the calculated energies for Mn1(II)−Fe2(II)-E and Fe1(II)−Mn2(II)-E models are essentially the same. The energy of Fe1(II)−Mn2(II)-M is only 1.7 kcal mol^{-1} lower than that of Mn1(II)−Fe2(II)-M, which cannot lead to a definitive conclusion that the reduced *Ct*-R2 is in Fe1(II)−Mn2(II) form.

From the energetic point of view, the Mn1(II)−Fe2(II) and Fe1(II)−Mn2(II) active site structures may coexist. However from a kinetic point of view, a predominance of one over another, can be determined by the protein environment at the metal insertion stage and by the metal insertion mechanism. As Jiang et al. pointed out,[39] experimentally it is a challenge to prepare the pure active form of *Ct*-R2 samples with only the Mn(II)−Fe(II) but not Mn(II)−Mn(II) and Fe(II)−Fe(II) active sites. Once the Fe(II)−Fe(II)-*Ct*-R2 is formed, it is quite reactive to O_2, and produces the Fe(III)−Fe(III)-*Ct*-R2,[39] which is the diiron inactive form that was characterized crystallographically (PDB code: 1SYY).[33] With an excess of Mn(II), the Mn(II)−Mn(II)-*Ct*-R2 complex can be formed, but this complex is labile and unreactive to O_2.[39] Therefore, use of excess Mn(II) does not prevent formation of the active Mn(II)−Fe(II) cofactor.[39] The current procedure of Jiang et al. and Younker et al.,[39,42,46] for preparing the active protein is to add 1.5 equiv of Mn(II) to an air-saturated solution of 370 μM (monomer concentration) apo-R2 at 5 °C, and then to slowly add 0.75 equiv per monomer Fe(II) (either natural abundance or ∼95% ^{57}Fe-enriched) over a period of 20 min.[39,42,46] Their earlier publications mention a different procedure, which includes premixing of Mn(II) and Fe(II) ions before being added to the metal-depleted R2.[40] In that case, Mn(II) is also 2-fold excess (1.0 equiv) over Fe(II) (0.5 equiv).

If the metal-binding affinity of one of the two sites is higher than the other because of the local and the extended protein environment, then Mn(II) will bind there preferentially when it is added prior to Fe(II). (Note that even when Mn(II) and Fe(II) are added together, Mn(II) is in 2-fold excess over Fe(II).) Later when Fe(II) is added, it will bind to the other site which is still open, or, if Mn(II) is present in both sites, displace the Mn(II) in the site of lower metal-binding affinity. (Recall that the Mn(II)−Mn(II)-*Ct*-R2 complex is labile.) To test this idea, we deleted the Fe1 or Fe2 in the four Mn1(II)−Fe2(II)-E, Fe1(II)−Mn2(II)-E, Mn1(II)−Fe2(II)-M, and Fe1(II)−Mn2(II)-M model structures, and calculated their relative energies. The four structures with Fe(II) deleted are called Mn1(II)-E, Mn2(II)-E, Mn1(II)-M, and Mn2(II)-M, correspondingly. The detailed calculations for these mono-Mn(II) structures are given in section 4.2.

4.2. Mono-Mn(II) State: Mn1(II)-E, Mn2(II)-E, Mn1(II)-M, and Mn2(II)-M. Currently no crystal structure of *Ct*-R2 with only one bound metal ion (Fe or Mn) is available. There is a crystal structure (PDB code: 1XSM, resolution 2.3 Å) of mouse RNR-R2 which contains one iron ion bound at metal site 2 (see Figure 9).[106] This structure is very similar to the reduced diferrous form of *E. coli* R2, but with site 1 open and with Glu267 (analogous to Glu238 in *E. coli* R2 and Glu227 in *Ct*-R2) binding to Fe2 in bidentate mode.

Previous wild-type and mutant apo *E. coli* R2 crystal structures show that the iron-free proteins do not undergo any major structural changes compared with the iron-containing R2.[107,108] Without iron ions, some of the potential unfavorable carboxylate interactions caused by electrostatic repulsion at the site are probably shielded by carboxylate-carboxylate hydrogen bonds (a proton may be shared by two adjacent carboxylate groups) or by the introduction of an intervening water molecule.[108] Also the two active site histidines may be in the protonated imidazolium form. However, the relevant crystallization experiments for apo *E. coli* R2 were performed at acid pH = 6, which favors protonation. In the mouse R2 single-Fe crystal structure, no water molecules were reported within the first coordination spheres of the iron sites.[106] The side chain of Asp139 (see Figure 9) (analogous to Glu89 in *Ct*-R2) at site 1 was seen further away from the metal site.[106] There is no direct evidence to show whether His173 and Asp139 (corresponding to His123 and Glu89 in *Ct*-R2) in the open site 1 are protonated or not. Even if His173 and Asp139 were protonated in the crystal structure, noting that these crystals were prepared at pH 4.7, these groups may not remain protonated at neutral pH. Therefore in the current study for the mono-Mn(II) states of *Ct*-R2 generated by the Fe(II) deletions described above, we treat both sites equally, and do not add extra explicit water molecules or change the protonation state of the residue side chains in the open site. First we deleted the Fe(II) from the Mn(II)−Fe(II) optimized model geometries. Since one of the water molecules in the optimized Mn1(II)−Fe2(II)-M and Fe1(II)−Mn2(II)-M structures is very far

(106) Kauppi, B.; Nielsen, B. A.; Ramaswamy, S.; Larsen, I. K.; Thelander, M.; Thelander, L.; Eklund, H. *J. Mol. Biol.* **1996**, *262*, 706–720.
(107) Aberg, A.; Nordlund, P.; Eklund, H. *Nature* **1993**, *361*, 276–278.
(108) Andersson, M. E.; Hogbom, M.; Rinaldo-Matthis, A.; Blodig, W.; Liang, Y. H.; Persson, B. O.; Sjoberg, B. T.; Su, X. D.; Nordlund, P. *Biochemistry* **2004**, *43*, 7966–7972.

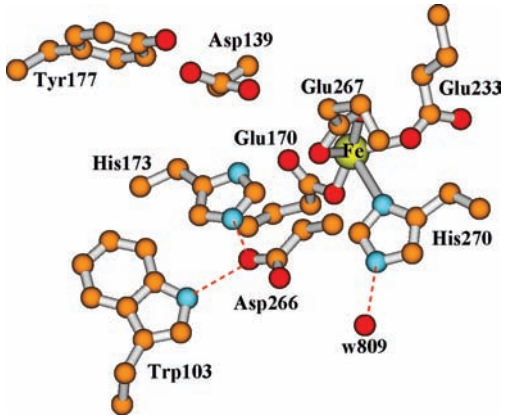

Figure 9. Active site of the crystal structure (PDB code: 1XSM) of mouse RNR-R2 with one iron ion bound at metal site 2.[106].

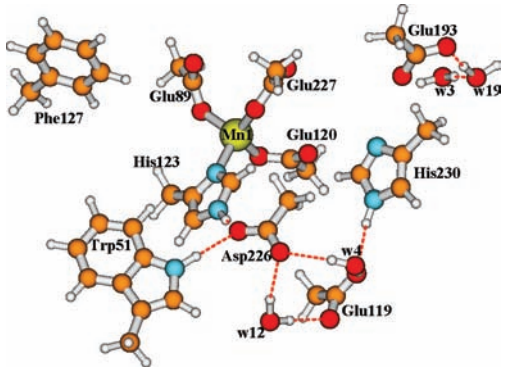

Figure 10. Optimized structure of Mn1(II)-E.

from the metal site 1 and may not be present in the active site (see Figure 8), we also deleted this water molecule from the Mn(II)-M models. COSMO geometry optimizations were then performed on these mono-Mn(II) models by the same methods as for the original Mn(II)−Fe(II) structures. However, the COSMO geometry optimizations on these large single-Mn(II) models proved computationally extremely slow for rearrangement of the residue side chains around the site where Fe(II) was removed. Therefore, the quantum cluster size was reduced by deleting the components of Arg225, Arg115, Asn50, and their surrounding water molecules (Figure 5), while the polarity of the dielectric medium in COSMO calculations was increased. The dielectric constant $\varepsilon = 32.6$ (for methanol) was chosen for COSMO geometry optimizations, since it is somewhat in between the low dielectric ($\varepsilon = 4.0$) and water ($\varepsilon = 80.0$) environment. Note that only in this subsection, the quantum clusters are smaller and the dielectric constant used in DFT-COSMO geometry optimizations is 32.6.

The optimized structures of Mn1(II)-E, Mn2(II)-E, Mn1(II)-M, and Mn2(II)-M are shown in Figures 10−13, respectively. We note that structures Mn1(II)-M and Mn2(II)-M contain one more water molecule than Mn1(II)-E and Mn2(II)-E. Therefore, direct energy comparisons can be made within the Mn(II)-M set and within the Mn(II)-E set, but not between Mn(II)-M and Mn(II)-E structures.

During the optimization in Mn1(II)-M, the side chain of Glu227 moved closer and bonded to Mn1, and the other

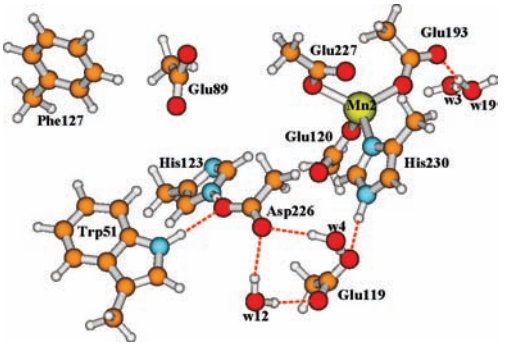

Figure 11. Optimized structure of Mn2(II)-E.

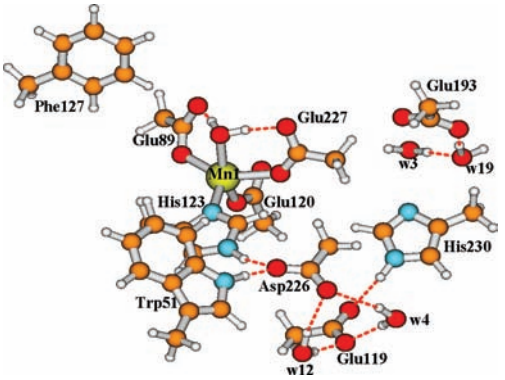

Figure 12. Optimized structure of Mn1(II)-M.

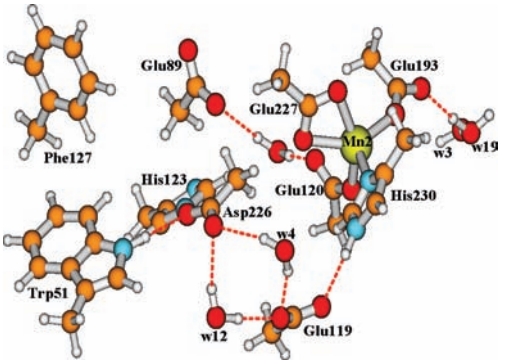

Figure 13. Optimized structure of Mn2(II)-M.

oxygen atom of Glu227 H-bonded to the ligand water molecule. The corresponding water molecule in Mn2(II)-M was moved between Glu89 and Glu120 since this structure had lower energy. The electronic energies of the four solvated mono-Mn(II) models after COSMO geometry optimizations are given in the last row of Table 2. The cluster Mn2(II)-E is by 0.54 eV (12.45 kcal mol^{-1}) lower than Mn1(II)-E. This is probably because the Glu227 side chain in Mn2(II)-E is nearly in the bidentate binding position, which is similar to Mn2(II)-M. Note that the corresponding carboxylate group (Glu267) in the single-Fe mouse R2 crystal structure (Figure 9) also has the bidentate binding position to Fe2.[106] The overall positions of the first shell ligand side chains in our optimized Mn2(II)-E and Mn2(II)-M structures are very similar to those in the Fe2-bound mouse R2. The Mn(II)-ligand coordination numbers in both Mn1(II)-M and Mn2(II)-M are 5, and

Table 2. DFT/PB-SCRF Calculations at the COSMO Optimized Geometries of the Mono-Mn(II) Models Mn1(II)-E, Mn2(II)-E, Mn1(II)-M, and Mn2(II)-M[a]

	Mn1(II)-E	Mn2(II)-E	Mn1(II)-M	Mn2(II)-M
E^{i}_{0} [b]	−693.78	−694.13	−709.48	−708.68
E_{strain} [c]	1.47	2.21	1.81	1.74
E^{f}_{0} [d]	−692.31	−691.92	−707.67	−706.94
$E^{f}_{protein}$ [e]	0.3	−39.0	−7.2	−28.0
$E^{f}_{reaction}$ [f]	−454.4	−454.0	−423.0	−452.6
$E_{PB\text{-}SCRF(total)}$ [g]	−712.00	−713.30	−726.33	−727.78
E_{COSMO} [h]	−713.45	−713.99	−728.38	−728.35

[a] Figures 10−13. [b] Initial (i) gas-phase electronic energy (eV) of the quantum cluster from DFT at the COSMO optimized geometry. [c] The electronic energy change (eV) during the whole SCRF cycle, $E_{strain} = E^{f}_{0} - E^{i}_{0}$, which is the energy cost of cluster polarization. [d] The quantum cluster electronic energy (eV) from DFT at the end of the DFT/PB-SCRF cycle, where the electron orbitals and density are polarized by the protein and solvent (f denotes final orbitals). [e] The final protein field energy (kcal mol^{-1}), obtained from the charge−charge interactions between the active site and the protein charges, screened by the different dielectric media (ε = 1.0 in quantum cluster, ε = 4.0 in protein, and ε = 80 in solvent). [f] The final reaction field energy (kcal mol^{-1}), obtained from the interaction between the active site charges (where ε = 1.0) and the dielectric solvent (ε = 80.0) and protein (ε = 4.0) environment. [g] $E_{PB\text{-}SCRF(total)} = E^{f}_{0} + E^{f}_{protein} + E^{f}_{reaction}$ (eV). [h] E_{COSMO} (eV) is the energy obtained from the COSMO geometry optimization (with ε = 32.6) including solvation.

their COSMO energies are essentially the same, with Mn1(II)-M lower than Mn2(II)-M by less than 1 kcal mol^{-1}. Therefore it is hard to determine whether Mn(II) favors binding at site 1 or site 2 by the calculations on the small active site clusters with continuum solvent models. The asymmetric protein environment should play an important role in this determination.

Before performing the protein plus solvent PB-SCRF calculations, we first performed a PB-SCRF calculation on the COSMO optimized structure of Mn1(II)-M (as an example) with only the reaction field (without protein) and with ε = 32.6. The final DFT/PB-SCRF energy is −728.34 eV, which is almost the same as the corresponding COSMO energy of −728.38 eV. Therefore the solvation effect in COSMO calculations is very similar to that in the DFT/PB-SCRF calculations (without protein field). Similar results were also observed previously.[71] Now the protein plus solvent PB-SCRF calculations are applied on the four mono-Mn(II) COSMO optimized geometries, as described in section 3.5.

The energy terms obtained from the PB-SCRF calculations are given in Table 2. (Some further protein and reaction field energy breakdowns are given in the Supporting Information, Table S1.) The definitions of these energy terms are given in the footnotes under Table 2. The initial gas-phase electronic energy (E^{i}_{0}, eV) of Mn2(II)-E is lower than Mn1(II)-E. After polarization by the protein and solvent, the final electronic energies E^{f}_{0} of Mn1(II)-E and Mn1(II)-M are lower than the corresponding energies of Mn2(II)-E and Mn2(II)-M by 0.39 eV (9.0 kcal mol^{-1}) and 0.73 eV (16.8 kcal mol^{-1}), respectively. However, the protein field charges strongly favor Mn(II) binding at site 2, since the $E^{f}_{protein}$'s of Mn2(II)-E and Mn2(II)-M are lower than those of Mn1(II)-E and Mn1(II)-M by 39.3 and 20.8 kcal mol^{-1}, respectively. The $E^{f}_{reaction}$'s of Mn1(II)-E and Mn2(II)-E are almost the same. For Mn1(II)-M and Mn2(II)-M, the $E^{f}_{reaction}$ further stabilizes Mn(II) binding at site 2. Finally, the total energies $E_{PB\text{-}SCRF(total)} = E^{f}_{0} + E^{f}_{protein} + E^{f}_{reaction}$ (eV) of Mn2(II)-E and Mn2(II)-M are lower than Mn1(II)-E and Mn1(II)-M by 1.30 eV (30.0 kcal mol^{-1}) and 1.45 eV (33.4 kcal mol^{-1}), respectively.

Since the protein structure is obtained from the diferric *Ct*-R2 state, and the four optimized active site structures here are only our best estimates of how Mn(II) binds to one of the two metal sites in *Ct*-R2, we cannot be sure if the mono-Mn(II) binding at site 2 is really lower by nearly 30 kcal mol^{-1} in energy compared to binding at site 1. However, such a large energy difference does indicate that the protein environment favors the mono-Mn(II) binding to site 2. Later when Fe(II) is added, Fe(II) then will bind to site 1, or replace the Mn(II) at site 1 if Mn(II)−Mn(II) complex is formed. We therefore propose that, if the Mn(II)−Fe(II) *Ct*-R2 protein is prepared with prior addition of Mn(II) or with Mn(II) excess over Fe(II), the active site is likely in the Fe1(II)−Mn2(II) form. The conclusion that site 2 has higher metal binding affinity in *Ct*-R2 is consistent with the observation in the single-Fe mouse R2 crystal structure where Fe binds at site 2.

Very recently, a protein Rv0233 dimer from *Mycobacterium tuberculosis* was solved by X-ray crystallography (PDB ID: 3EE4).[109] This protein was found also containing a Mn−Fe center which is similar to *Ct*-R2. The function of Rv0233 is still not known. The X-ray structure was probably determined in the Mn(III)−Fe(III) state. A striking difference compared to R2 proteins is that there is a bound ligand in Rv0233 that coordinates directly to the metal site and is modeled as myristic (C_{14}) acid.[109] A tyrosine(162)-valine(71) cross-link is also found in the Rv0233 active site, which is likely generated during one of the first redox cycles of the metal site.[109] According to the first and second ligand-shell similarities on the residue types, the metal sites 1 and 2 in Rv0233 also relate to the sites 1 and 2 in *Ct*-R2, respectively. In Rv0233, the anomalous diffraction difference maps show that the Mn ion specifically occupies metal site 1, which is the opposite of what we have just proposed for the metal binding assignment for *Ct*-R2. However, even though there are structural similarities between the active sites of Rv0233 and *Ct*-R2, the site of metal binding is highly dependent on the longer-range protein and solvent environment (as studied above), and on the metal insertion process. One cannot simply draw the conclusion that Mn will also occupy metal site 1 in *Ct*-R2 solely on the grounds that Mn was found to be at site 1 in Rv0233. It is another challenge to understand why Mn1−Fe2 is specifically formed in Rv0233. In principle we can perform similar calculations on Rv0233 to those we have performed on *Ct*-R2. However, additional uncertainties exist for the reduced state active site structure of Rv0233. For example, we do not know if the myristic acid ligand also binds to the Mn(II)−Fe(II) center, what the states are corresponding to the positions of Tyr162 and Val71 prior to their two electron oxidation reaction and cross-linkage, or how to construct the Mn(II)−Fe(II) active site of Rv0233 based on its Mn(III)−Fe(III) X-ray structure. Therefore in the current study, we only focus on the *Ct*-R2 active site calculations.

Once the Fe and Mn positions are determined in the Mn(II)−Fe(II) state, they are likely to be locked during

(109) Andersson, C. S.; Högbom, M. *Proc. Natl. Acad. Sci. U.S.A.* **2009**, *106*, 5633–5638.

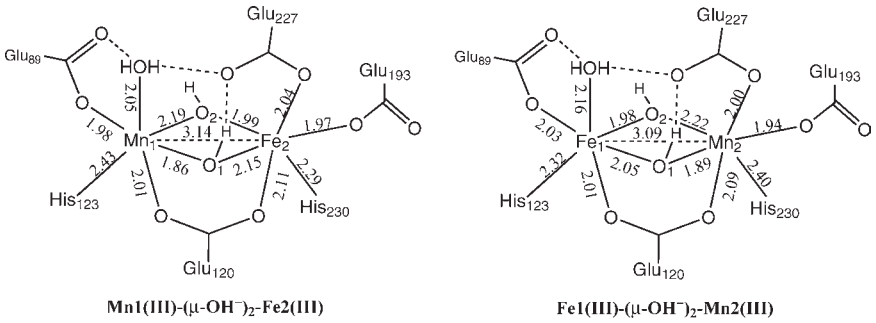

Figure 14. Main metal−ligand distances in the DFT(OPBE) optimized *Ct*-R2 Mn1(III)-(μ-OH$^-$)$_2$-Fe2(III) and Fe1(III)-(μ-OH$^-$)$_2$-Mn2(III) model structures. The residues in the outer shells of the active site models are shown in Figures 4 and 5.

Table 3. Calculated Mössbauer Isomer Shifts (δ, mm s^{-1}), Quadrupole Splittings (ΔE_Q, mm s^{-1}), η, Hyperfine Coupling Constants (A, MHz),[a] Net Spin Populations (NSP), *J* Coupling Constants (cm^{-1}), Spin Projected Energies (E_0, eV), and Mn−Fe Distances (r, Å) for the Active Site Models of Mn1(III)-(μ-OH$^-$)$_2$-Fe2(III) and Fe1(III)-(μ-OH$^-$)$_2$-Mn2(III), and Compared with Experimental (Exp) Results

	Mn1(III)-(μ-OH$^-$)$_2$-Fe2(III)		Fe1(III)-(μ-OH$^-$)$_2$-Mn2(III)		exp[b]	
	Mn1	Fe2	Fe1	Mn2	Mn	Fe
δ		0.56	0.53			0.51[c]
ΔE_Q		0.37	0.60			0.81
η		0.66	0.74			
A_1	84.02	−55.96	−55.23	93.40	269	−64.5
A_2	193.62	−55.56	−54.52	198.18	392	−64.5
A_3	133.27	−54.35	−52.86	138.93	314	−64.5
A^{iso}	136.97	−55.29	−54.20	143.51	325	−64.5
A_1^{aniso}	−52.95	−0.67	−1.03	−50.10	−56	0.0
A_2^{aniso}	56.65	−0.27	−0.31	54.67	67	0.0
A_3^{aniso}	−3.70	0.94	1.34	−4.57	−11	0.0
NSP	−4.03	4.16	4.18	−4.03		
J	−30		−35			
E_0	−1079.3002		−1079.3773			
r(Mn−Fe)	3.14		3.09		2.90	

[a] DFT-calculated A-tensors were rescaled by the spin coupling factors (see text). A^{iso} represents the isotropic A-tensor, and A^{aniso} stands for the anisotropic A-tensor component. [b] Mössbauer and hyperfine experimental data are from ref 38, and the EXAFS Mn−Fe distance is taken from ref 44. [c] The reported experimental isomer shift is 0.43 mm s^{-1} obtained at 190 K.[38] We have shifted it to 0.51 mm s^{-1} at 4.2 K taking account of the second-order Doppler effect.

the whole catalytic process. Next we will see if the Fe1(II)−Mn2(II) assignment in *Ct*-R2 is supported by the Mössbauer and hyperfine calculations on other higher oxidation states.

4.3. Mn(III)−Fe(III) State: Mn1(III)-(μ-OH$^-$)$_2$-Fe2(III) and Fe1(III)-(μ-OH$^-$)$_2$-Mn2(III). Mn1(III)-(μ-OH$^-$)$_2$-Fe2(III) and Fe1(III)-(μ-OH$^-$)$_2$-Mn2(III) models are shown in Figures 4 and 5. The main bond lengths around the metal centers of the optimized geometries are given in Figure 14. Other calculated properties are given in Table 3.

Similar to the Mn(II)−Fe(II)-M model calculations, the spin-projected energy of Fe1(III)-(μ-OH$^-$)$_2$-Mn2(III) model is also lower than Mn1(III)-(μ-OH$^-$)$_2$-Fe2(III) by about 1.8 kcal mol^{-1}.

The reported ^{57}Fe Mössbauer isomer shift 0.43 mm s^{-1} was measured at 190 K.[38] We now shift it to 0.51 mm s^{-1} at the common temperature of 4.2 K, by taking account of the second-order Doppler effect (0.43 + 0.12(190 − 4.2)/(300 − 4.2) mm s^{-1}).[51,110,111] The calculated isomer shift 0.53 mm s^{-1} for Fe on site 1 in Fe1(III)-(μ-OH$^-$)$_2$-Mn2(III) is by 0.03 mm s^{-1} closer to the experimental value of 0.51 mm s^{-1} than the Mn1(III)-(μ-OH$^-$)$_2$-Fe2(III) model. The calculated quadrupole splitting 0.60 for Fe1(III)-(μ-OH$^-$)$_2$-Mn2(III) is much closer to the observed value of 0.81 mm s^{-1} than that (0.37 mm s^{-1}) of the Mn1(III)-(μ-OH$^-$)$_2$-Fe2(III) structure. The standard deviation (SD) of ΔE_Q for OPBE on the test set of synthetic complexes is 0.25 mm s^{-1},[51] so the first calculated value (0.60 mm s^{-1}) is less than 1 SD from experiment, while the second (0.37 mm s^{-1}) is nearly 2 SD from experiment. Therefore, both the energetic and Mössbauer calculations favor the active site of the Mn(III)−Fe(III) state of *Ct*-R2 being represented by the Fe1(III)-(μ-OH$^-$)$_2$-Mn2(III) model structure.

Both experimental ^{57}Fe and ^{55} Mn hyperfine coupling constants are available for *Ct*-R2 in Mn(III)−Fe(III) state.[38] The measured ^{57}Fe hyperfine A-tensor is very isotropic (−64.5, −64.5, −64.5 MHz), typical for Fe(III) site. The calculated A-tensors for Fe1 in Fe1(III)-(μ-OH$^-$)$_2$-Mn2(III) and Fe2 in Mn1(III)-(μ-OH$^-$)$_2$-Fe2(III) are almost the same, and also very isotropic. Theoretically it is very difficult to predict the absolute value of the isotropic hyperfine coupling constants of metal centers.[26,92,112,113] Normally the anisotropic components (A^{aniso}) can be more accurately predicted by the DFT calculations. Our

(110) Fee, J. A.; Findling, K. L.; Yoshida, T.; Hille, R.; Tarr, G. E.; Hearshen, D. O.; Dunham, W. R.; Day, E. P.; Kent, T. A.; Munck, E. *J. Biol. Chem.* **1984**, *259*, 124–133.
(111) Liu, T. Q.; Lovell, T.; Han, W. G.; Noodleman, L. *Inorg. Chem.* **2003**, *42*, 5244–5251.
(112) Noodleman, L.; Baerends, E. J. *J. Am. Chem. Soc.* **1984**, *106*, 2316–2327.
(113) Neese, F. *J. Chem. Phys.* **2003**, *118*, 3939–3948.

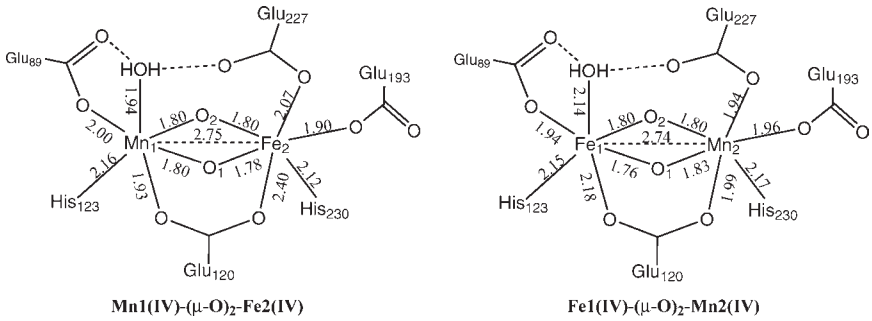

Figure 15. Main metal−ligand distances in the DFT(OPBE) optimized *Ct*-R2 Mn1(IV)-(μ-O)$_2$-Fe2(IV) and Fe1(IV)-(μ-O)$_2$-Mn2(IV) model structures. The residues in the outer shells of the active site models are shown in Figures 4 and 5.

previous PW91 calculated ^{57}Fe isotropic hyperfine coupling constants (A^{iso}) are less than half of the observed ones.[26] Current OPBE calculated ^{57}Fe A^{iso}'s for both models are much closer to (about 85% of) the experimental data. The almost zero anisotropic components of the ^{57}Fe A-tensors are very well reproduced in both structures. The predicted A^{iso} for Mn2 site (143.51 MHz) is by about 7 MHz larger than for Mn1 (136.97 MHz). However, both values are still small (about 42−44%) compared with the measured one (325 MHz). The two models yield almost the same predicted anisotropic components of the ^{55} Mn A-tensors, which are also in very good agreement with the corresponding experimental values.

The diiron center in the diferric *Ct*-R2 X-ray crystal structure (resolution 1.7 Å) is very symmetric, with 2.1 Å for Fe1−O1 and Fe2−O1 distances, and 2.2 Å for Fe1−O2 and Fe2−O2. However, with one of the iron sites replaced by Mn, the center core is more asymmetric (less rhombic), with Mn−O1 and Fe−O2 shorter than Mn−O2 and Fe−O1. The very short Mn−O distance ~1.65 Å reported from EXAFS[44] is not reproduced. The shortest calculated Mn−O distances here are 1.86 Å for Mn1−O1 and 1.89 Å for Mn2−O1. The calculated Mn−Fe distances for the Mn1−Fe2 and Fe1−Mn2 models are almost the same (about 3.1 Å), with only 0.05 Å difference. These calculated Mn−Fe distances are a little shorter than the Fe−Fe distance (3.3 Å) in the diferric *Ct*-R2 X-ray crystal structure.

Summarizing the *Ct*-R2 Mn(III)−Fe(III) state calculations, the relative energies, Mössbauer isomer shifts and quadrupole splittings favor the Fe1-(μ-OH$^-$)$_2$-Mn2 structure over the Mn1(III)-(μ-OH$^-$)$_2$-Fe2(III) model, which supports the proposed metal assignment made in section 4.2.

4.4. Superoxidized Mn(IV)−Fe(IV) State: Mn1(IV)-(μ-O)$_2$-Fe2(IV) and Fe1(IV)-(μ-O)$_2$-Mn2(IV). The main metal−ligand distances in the first shell of the optimized Mn1(IV)-(μ-O)$_2$-Fe2(IV) and Fe1(IV)-(μ-O)$_2$-Mn2(IV) structures are given in Figure 15. So far there are no EXAFS experimental data available for the Mn(IV)−Fe(IV) state of *Ct*-R2. Comparing with the calculated Mn(III)−Fe(III) state, the Mn(IV)−Fe(IV) distance is much shorter (by about 0.3 Å). The shortest metal−ligand distance is Fe(IV)−O1, 1.76 Å for Fe1−O1 and 1.78 Å for Fe2−O1.

Other calculated properties including the Mössbauer isomer shifts and quadrupole splittings, hyperfine coupling constants, and spin projected energies for these two Mn(IV)−Fe(IV) models are given in Table 4. Unlike the Mn(III)−Fe(III) state, the Fe1(IV)-(μ-O)$_2$-Mn2(IV) model is now in higher energy than the Mn1(IV)-(μ-O)$_2$-Fe2(IV) structure by 1.7 kcal mol^{-1}. However, the metal sites in the superoxidized state are not expected to be labile.

Table 4. Calculated Mössbauer Isomer Shifts (δ, mm s^{-1}), Quadrupole Splittings (ΔE_Q, mm s^{-1}), η, Hyperfine Coupling Constants (A, MHz),[a] Net Spin Populations (NSP), *J* Coupling Constants (cm^{-1}), and Spin Projected Energies (E_0, eV) for the Active Site Models of Mn1(IV)-(μ-O)$_2$-Fe2(IV) and Fe1(IV)-(μ-O)$_2$-Mn2(IV), and Compared with Experimental (Exp) Results

	Mn1(IV)-(μ-O)$_2$-Fe2(IV)		Fe1(IV)-(μ-O)$_2$-Mn2(IV)		exp[b]	
	Mn1	Fe2	Fe1	Mn2	Mn	Fe
δ		0.24	0.23			0.17
ΔE_Q		0.47	0.76			0.75
η		0.43	0.79			0.64
A_1	130.10	−35.25	−33.53	135.84	247	−55.9
A_2	113.38	−38.83	−39.08	120.98	216	−59.3
A_3	122.41	−20.32	−19.69	125.54	243	−40.5
A^{iso}	121.97	−31.47	−30.76	127.45	235.3	−51.9
A_1^{aniso}	8.14	−3.78	−2.76	8.39	11.7	−4.0
A_2^{aniso}	−8.59	−7.36	−8.31	−6.48	−19.3	−7.4
A_3^{aniso}	0.45	11.14	11.07	−1.91	7.7	11.4
NSP	−2.95	3.25	3.22	−3.00		
J	−232		−226			
E_0	−1070.4874		−1070.4144			

[a] DFT-calculated A-tensors were rescaled by the spin coupling factors (see text). A^{iso} represents the isotropic A-tensor, and A^{aniso} stands for the anisotropic A-tensor component. [b] Mössbauer and hyperfine experimental data are from ref 40. The original experimental ^{57}Fe Mössbauer quadrupole splitting was reported as $\Delta E_Q = -0.75$ mm s^{-1} with $\eta = -10$. The data shown in the table are obtained after reordering the eigenvalues of the *V* tensors.

The calculated Mössbauer isomer shifts for ^{57}Fe in the two Mn(IV)−Fe(IV) models (0.24 and 0.23 mm s^{-1}) are almost the same and close to the experimental value of 0.17 mm s^{-1}, representing the high-spin Fe(IV) sites. The experimentally reported ΔE_Q is −0.75 mm s^{-1} with η = −10. If we trace back to reorder the eigenvalues as $|V_{zz}| \geq |V_{yy}| \geq |V_{xx}|$, we will have $\Delta E_Q = 0.75$ mm s^{-1} and η = 0.64. The predicted ΔE_Q for the two models are very different. The predicted $\Delta E_Q = 0.47$ mm s^{-1} for Fe2 in Mn1(IV)-(μ-O)$_2$-Fe2(IV) is much smaller than the experimental result, 0.75 mm s^{-1}. By contrast, the predicted $\Delta E_Q = 0.76$ mm s^{-1} for Fe1 in Fe1(IV)-(μ-O)$_2$-Mn2(IV) almost exactly reproduces the experimental value, 0.75 mm s^{-1}. Therefore the Mössbauer property calculations for the Mn(IV)−Fe(IV) state also favor the proposition that Fe is located at site 1.

Similarly to the Mn(III)−Fe(III) state, switching the Mn and Fe positions in Mn(IV)−Fe(IV) state does not make a significant change in the calculated hyperfine A-tensor. The predicted anisotropic components of the ^{57}Fe A-tensor of both models are in good agreement with

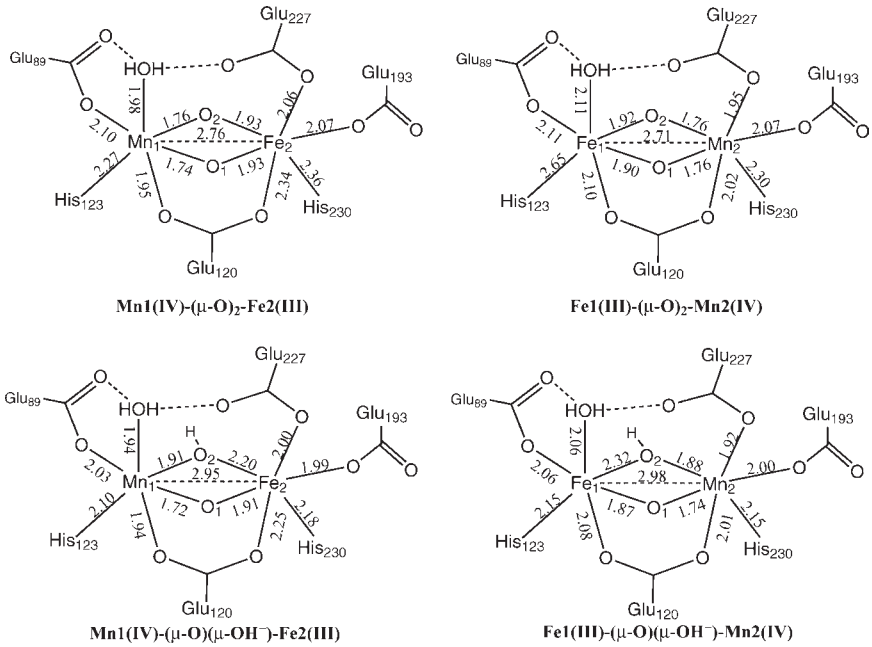

Figure 16. Main metal−ligand distances in the DFT(OPBE) optimized *Ct*-R2 Mn1(IV)-(μ-O)$_2$-Fe2(III), Fe1(III)-(μ-O)$_2$-Mn2(IV), Mn1(IV)-(μ-O)(μ-OH$^-$)-Fe2(III), and Fe1(III)-(μ-O)(μ-OH$^-$)-Mn2(IV) model structures. The residues in the outer shells of the active site models are shown in Figures 4 and 5.

experiment. However, the experimental anisotropic components of the ^{55}Mn A-tensor, especially A_2^{aniso} and A_3^{aniso} are not well reproduced by the two models. This may be because the models deviate from the real *Ct*-R2 Mn(IV)−Fe(IV) structure, or simply because of the accuracy limitation of our A-tensor calculations for Mn(IV). Notice that experimentally the largest A^{aniso} value for Mn(IV) is less than 10% of the isotropic value, while for Fe(IV) A^{aniso}(largest) is about 20% compared to A^{iso}. Therefore, computationally it is easier to predict more accurately the A^{aniso} values for Fe(IV) than for Mn(IV).

4.5. Oxidized Mn(IV)−Fe(III) state: Mn1(IV)-(μ-O)$_2$-Fe2(III), Fe1(III)-(μ-O)$_2$-Mn2(IV), Mn1(IV)-(μ-O)(μ-OH$^-$)-Fe2(III), and Fe1(III)-(μ-O)(μ-OH$^-$)-Mn2(IV). Very recently, we have studied the feasible active site structures for the Fe(IV)−Fe(III) intermediate X state of *E. coli* RNR.[30] Calculations show that the di-μ-oxo model of Fe1(III)-(μ-O)$_2$-Fe2(IV) is more consistent with ENDOR experiments.[17] However, energetically the bridging oxo and hydroxo form of Fe1(III)-(μ-O)(μ-OH$^-$)-Fe2(IV) is favored for some active site models. Further calculations show that if a sulfate ion (taking sulfate as an example, since sulfate ions certainly exist in the buffer of the ENDOR experiment) interacts with Arg236 (see Figure 3), the carboxylate group of Asp237 tends to be protonated, and once Asp237 is protonated, the Fe(III)Fe(IV) center in *E. coli* RNR-X favors the di-μ-oxo structure. In the present case, by comparing the calculated properties with experiment, we will also analyze whether the di-μ-oxo or the (μ-oxo)(μ-hydroxo) form is likely to represent the Mn(IV)Fe(III) active site center of *Ct*-R2.

Two different Mn(IV)−Fe(III) distances, 2.75 Å[44] and 2.92 Å,[42] were reported from EXAFS experiments by two research groups. Younker et al.[42] also reported the presence of a short 1.74 Å Mn(IV)−O bond length from the Mn edge data. The calculated (Figure 16) Mn(IV)−Fe(III) distances (2.76 and 2.71 Å) in the di-μ-oxo models Mn1(IV)-(μ-O)$_2$-Fe2(III) and Fe1(III)-(μ-O)$_2$-Mn2(IV) are short, and are consistent with the 2.75 Å EXAFS result. On the other hand, the Mn1(IV)-(μ-O)(μ-OH$^-$)-Fe2(III) and Fe1(III)-(μ-O)(μ-OH$^-$)-Mn2(IV) models yield longer Mn−Fe distances (2.95 and 2.98 Å, respectively), which agree with the experimental 2.92 Å very well. In the optimized Mn1(IV)-(μ-O)$_2$-Fe2(III) and Fe1(III)-(μ-O)$_2$-Mn2(IV) structures, both Mn−O1 and Mn−O2 are short and have about the same bond lengths (1.74−1.76 Å). In models Mn1(IV)-(μ-O)(μ-OH$^-$)-Fe2(III) and Fe1(III)-(μ-O)(μ-OH$^-$)-Mn2(IV), only one Mn−O1 bond is short (1.72−1.74 Å), which agrees with the Mn EXAFS data from Younker et al. where only a single O scatterer at 1.74 Å was found.[42] Therefore, Mn1(IV)-(μ-O)(μ-OH$^-$)-Fe2(III) or Fe1(III)-(μ-O)(μ-OH$^-$)-Mn2(IV) is more like the active site structure observed from the latter EXAFS experiment.[42]

Other calculated properties of these four Mn(IV)−Fe(III) models are given in Table 5. The Mn1(IV)-(μ-O)$_2$-Fe2(III) model has a slightly larger predicted ^{57}Fe Mössbauer isomer shift value, 0.58 mm s^{-1}, than the other three models, which are all close to the observed value of 0.52 mm s^{-1}.[38] The calculated Fe quadrupole splitting values of the (μ-oxo, μ-hydroxo) models (−1.23 and −1.38 mm s^{-1}) are much larger than the corresponding results for the di-μ-oxo models (−0.82 and −0.78 mm s^{-1}), and much closer to the experimental observation (−1.32 mm s^{-1}) (note that the standard deviation of ΔE_Q from fit is 0.25 mm s^{-1}). The calculated pK_a's of site O2 also show that the (μ-oxo, μ-hydroxo) models are energetically far more stable than the corresponding di-μ-oxo models. Therefore, the (μ-oxo, μ-hydroxo) models are more likely to represent the active site structure of Mn(IV)−Fe(III) state of *Ct*-R2. Both theoretical studies by Roos and Siegbahn, and by Younker et al. have proposed that the *Ct*-R2 Mn(IV)−Fe(III) state has (μ-O) and (μ-OH$^-$) bridges.[42,45] Our combined results for geometries, energies, and protonation states of bridging oxygens support this proposed active site composition and the EXAFS result from Younker et al.[42] On purely

Table 5. Calculated Fe Mössbauer Isomer Shifts (δ, mm s^{-1}), Quadrupole Splittings (ΔE_Q, mm s^{-1}), η, Fe Hyperfine Coupling Constants (A, MHz),[a] Net Spin Populations (NSP), J Coupling Constants (cm^{-1}), Spin Projected Energies (E_0, eV), the pK_a of the Bridging OH^-, and Mn−Fe Distances (r, Å) for the Active Site Models of Mn1(IV)-(μ-O)$_2$-Fe2(III), Fe1(III)-(μ-O)$_2$-Mn2(IV), Mn1(IV)-(μ-O)(μ-OH^-)-Fe2(III), and Fe1(III)-(μ-O)(μ-OH^-)-Mn2(IV), and Compared with Experimental (Exp) Results

	Mn1(IV)-(μ-O)$_2$-Fe2(III)	Fe1(III)-(μ-O)$_2$-Mn2(IV)	Mn1(IV)-(μ-O)(μ−OH^-)-Fe2(III)	Fe1(III)-(μ-O)(μ−OH^-)-Mn2(IV)	exp [b]
δ(Fe)	0.58	0.53	0.54	0.49	0.52
ΔE_Q(Fe)	−0.82	−0.78	−1.23	−1.38	−1.32
η	0.93	0.74	0.24	0.83	0.11
A_1	−42.86	−41.14	−39.99	−36.35	−55.3
A_2	−41.33	−39.94	−38.08	−34.56	−53.5
A_3	−40.32	−38.32	−37.20	−32.95	−52.3
A^{iso}	−41.50	−39.8	−38.42	−34.62	−53.7
A_1^{aniso}	−1.36	−1.34	−1.57	−1.73	−1.6
A_2^{aniso}	0.17	−0.14	0.35	0.06	0.2
A_3^{aniso}	1.18	1.48	1.22	1.66	1.4
NSP(Mn)	−2.88	−2.91	−2.91	−2.97	
NSP(Fe)	4.06	4.04	4.08	4.09	
J	−153	−125	−160	−181	
E_0	−1074.4391	−1074.3623	−1075.0395	−1074.9881	
pK_a(OH^-)			20.30	20.73	
r(Mn−Fe)	2.76	2.71	2.95	2.98	2.75, 2.92 [c]

[a] DFT-calculated A-tensors were rescaled by the spin coupling factor (see text). A^{iso} represents the isotropic A-tensor, and A^{aniso} stands for the anisotropic A-tensor component. [b] Fe Mössbauer and hyperfine experimental data are from refs 39 and 42. The original experimental ^{57}Fe Mössbauer quadrupole splitting was reported as $\Delta E_Q = 1.32$ mm s^{-1} with $\eta = -2.6$.[39] The data shown in the table are obtained after reordering the eigenvalues of the V tensors.[42] [c] The EXAFS Mn−Fe distance 2.75 Å is taken from ref 44, and 2.92 Å from ref 42.

experimental grounds, the Mn(IV)−Fe(III) complex from Younker et al.[42] is about 85−90% pure based on their Mössbauer analysis (10−15% Fe(III)−Fe(III) contaminant). These samples are preferable to the physical mixtures of Mn−Fe oxidation states used for the EXAFS analysis of Mn(IV)−Fe(III) in ref 44.

Again as in the Mn(III)−Fe(III) and Mn(IV)−Fe(IV) calculations, the predicted ^{57}Fe A-tensor values for the four Mn(IV)−Fe(III) models are also very similar to each other, and all the predicted A^{aniso}'s are in good agreement with experiment. The absolute values of the A^{iso}'s obtained from our current OPBE calculations are similar to and some are even larger than those obtained by Younker et al. for their Mn(IV)−Fe(III) model A-tensor calculations using the B3LYP functional.[42]

As in the calculations performed by Younker et al.,[42] it is hard to determine whether Mn resides on site 1 or site 2 in the Mn(IV)-(μ-O)(μ-OH^-)-Fe2(III) state. If we have to choose one of the two, the Fe1(III)-(μ-O)(μ-OH^-)-Mn2(IV) model's ^{57}Fe quadrupole splitting property is a little closer to experiment. The calculations of Younker et al. using the B3LYP method always predict better isomer shifts when Fe is at site 1 for their different Mn(IV)−Fe(III) models.[42]

5. Conclusions

The R2 unit of *Chlamydia trachomatis* RNR contains a Mn−Fe active site and a phenylalanine (Phe127), rather than a diiron center and a tyrosine as found in conventional class-I RNRs. The first-shell ligand residue types and oxygen species of *Ct*-R2 are more like those of the diiron active site of MMOH. In the current paper, we have performed DFT broken-symmetry calculations on several *Ct*-R2 active site models, to discover which metal site is Mn versus Fe, to analyze potential protonation states of bridging oxygens, and to study the Mn−Fe active site structures, energetics, Mössbauer, and hyperfine properties of *Ct*-R2 in different oxidation states. These models are constructed for the reduced Mn(II)−Fe(II), met Mn(III)−Fe(III), superoxidized Mn(IV)−Fe(IV), and oxidized Mn(IV)−Fe(III) states according to the available diiron *Ct*-R2, *E. coli* R2 and MMOH X-ray crystal structures and previous intermediate state calculation models for *E. coli* R2 and MMOH. Both Mn1−Fe2 (site 1 is the metal site closer to Phe127) and Fe1−Mn2 structures for each model are studied.

The positions of Mn and Fe sites are very probably fixed during the sample preparation in the reduced state (by adding Mn(II) and Fe(II) into the metal-depleted R2).[38] Then they are not likely to switch positions based on the poorer lability of M(III) and M(IV) compared to M(II) for both Mn and Fe. It is therefore more important to compare the relative energies of the Mn1(II)−Fe2(II) and Fe1(II)−Mn2(II) structures. Our calculations show that for the reduced *Ct*-R2 structures which were established according to the diferrous active site of MMOH, the Fe1(II)−Mn2(II) active site is by 1.7 kcal mol^{-1} lower in energy than the corresponding Mn1(II)−Fe2(II) structure. On the basis of this energy difference, one cannot draw a definite conclusion that Fe is positioned on site 1. Since the current best procedure for preparing the Mn(II)−Fe(II) *Ct*-R2 sample is to add 2-fold excess Mn(II) to apo-R2 prior to adding Fe(II), to limit the formation of the Fe(II)−Fe(II) complex,[46] Mn(II) should bind first to the metal site which has higher metal-binding affinity determined by the local and the extended protein and solvent environment. We therefore studied how the protein and solvent environment influence the binding of mono-Mn(II) to site 1 or site 2 by performing the Poisson−Boltzmann self-consistent reaction field calculations on four mono-Mn(II) active site structures. Our current calculations indicate that the protein environment stabilizes the structures with mono-Mn(II) binding at site 2. We therefore propose that Mn(II) occupies site 2 and Fe(II) will occupy site 1 when it is added later. This Fe1−Mn2 assignment is supported by further Mössbauer calculations on other higher oxidation state active site models. The conclusion that site 2 has a higher metal binding affinity in *Ct*-R2 is consistent with the single-Fe containing crystal structure of mouse R2 where the Fe was found bound at site 2, and also consistent with the higher Fe(II) affinity at site Fe2 in *E. coli* R2 found by Bollinger et al.

based on their two-iron-isotope reaction and Mössbauer spectroscopy experiments.[114] In future work, we plan to analyze the likely protonation states of the apo-*Ct*-R2 structure, and the comparative energies of single-Mn(II) binding with associated proton exchange at alternative metal binding sites. Our calculations also support the conclusion that the Mn(IV)−Fe(III) active site contains μ-oxo and μ-hydroxo bridges, rather than two μ-oxo bridges.

(114) Bollinger, J. M.; Chen, S. X.; Parkin, S. E.; Mangravite, L. M.; Ley, B. A.; Edmondson, D. E.; Huynh, B. H. *J. Am. Chem. Soc.* **1997**, *119*, 5976–5977.

Acknowledgment. We thank NIH for financial support (GM43278 to L.N., GM086243 to D.B and D.A.G). D.A.G. and D.B. also thank the American Lebanese Syrian Associated Charities (ALSAC) for support.

Supporting Information Available: All optimized active site geometries in different oxidation states are given. More detailed protein and reaction field energy terms from the DFT/PB-SCRF calculations on the four mono-Mn(II) structures are given in Table S1. This material is available free of charge via the Internet at http://pubs.acs.org.